BIRZEIT UNIVERSITY

Deuteration effect on structure, magnetic and thermodynamic properties in spin-crossover compound $Fe(NCS)_2(PM\text{-}BiA)_2$

تأثير الديوتيريوم على البنية والخصائص المغناطيسية والديناميكية
الحرارية في مركب التقاطع الدوراني $Fe(NCS)_2(PM\text{-}BiA)_2$

Eman Raddad

Supervisor: Dr. Zafer Hawash
Co-Supervisor: Prof. Dr. Karen Friese, Forschungszentrum Jülich, Germany

June 2025

Deuteration effect on structure, magnetic and thermodynamic properties in spin-crossover compound Fe(NCS)$_2$(PM-BiA)$_2$

تأثير الديوتيريوم على البنية والخصائص المغناطيسية والديناميكية

الحرارية في مركب التقاطع الدوراني Fe(NCS)$_2$(PM-BiA)$_2$

Eman Raddad

Supervisor: Dr. Zafer Hawash
Co-Supervisor: Prof. Dr. Karen Friese, Forschungszentrum Jülich, Germany

This thesis was submitted in partial fulfillment of the requirements for the Master's Degree in Physics from the Faculty of Graduate Studies at Birzeit University, Palestine.

June 2025

Deuteration effect on structure, magnetic and thermodynamic properties in spin-crossover compound $Fe(NCS)_2(PM\text{-}BiA)_2$

تأثير الديوتيريوم على البنية والخصائص المغناطيسية والديناميكية الحرارية في مركب التقاطع الدوراني $Fe(NCS)_2(PM\text{-}BiA)_2$

Eman Raddad

Accepted by the Faculty of Graduate Studies, Birzeit University, in partial fulfillment of the requirements for the Master's Degree in Physics.
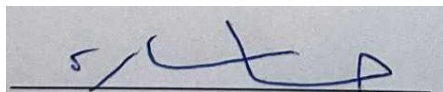
Thesis committee:

_____
Zafer Hawash, Ph.D. (Principal advisor)

_____
Abdallah Sayyed-Ahmad, Ph.D. (Member)

_____
Hazem Abu Sara, Ph.D. (Member)

June 2025

Acknowledgment

I am deeply grateful to God for granting me the health and strength necessary to complete this research.

I wish to express my sincere thanks to my supervisor, Dr. Zafer Hawash, for his continued encouragement and unwavering support. Additionally, I extend my heartfelt gratitude to Prof. Dr. Karen Friese, whose generous sharing of knowledge, sincere and constructive advice, and constant encouragement, particularly her year-long support in following up on my visa, are deeply appreciated.

I am also grateful to Dr. Ji Qi and Dr. Pulkit Prakash, whose scientific guidance and unwavering support greatly enriched my research experience. Their collaboration, expertise, and encouragement were instrumental in overcoming challenges throughout this work. Additionally, for the group members at JCNS-2, Dr. Hend Shahed, Prof. Dr. Manuel Angst, Dr. Jörg Voigt, and Jörg Perßon, for their advice and consultations during my thesis, and also for Dr. Kuno Schwärzer and Dr. Jürgen Allgaier from JCNS-1 for hosting me in their chemistry lab.

I take this opportunity to express gratitude to all of the physics department members for their help and support, and to all members of the Palestinian German Science Bridge (PGSB) for giving me this amazing opportunity. I also thank my parents for their unceasing encouragement, support, and attention. I am also grateful to my friends who supported me through this amazing experience.

Abstract

This thesis explores the role of the deuteration effect on the change of the structure, magnetic, and thermodynamic properties in spin crossover compound $Fe(NCS)_2(PM\text{-}BiA)_2$, where PM-BiA stands for pyridine-2-aldehyde-4-aminobiphenyl. In this study, the 4-aminobiphenyl was deuterated to 95.7% and engaged to form a partial ligand with pyridine-2-aldehyde. As a result, both orthorhombic and monoclinic polymorphs of the compound were synthesized in partial deuterated forms with some impurities and compared with the protonated form after characterization by X-ray diffraction, physical property measurement system, and differential scanning calorimetry.

Deuteration affects the transition temperature, leading to a reduction in the monoclinic phase and an increase in the orthorhombic phase when compared with the protonated ones. This could be attributed to deuteration lowering the energy required for the spin transition and altering the reduced mass, therefore influencing lattice vibrations. Moreover, the involvement of deuterated sites in hydrogen bonding contributes to an increase in the transition temperature.

The orthorhombic structure shows an increase in all lattice parameters compared to the monoclinic structure. The different behavior could be due to the difference in volume or density. Additionally, the deuteration leads to a significant reduction in enthalpy (ΔH) and entropy (ΔS) results, which could be due to lowered zero-point energy and weaker cooperative interactions.

These findings highlight the effect of deuteration on spin transition behavior and set the next steps for future work by full deuteration synthesis and single-crystal analysis.

الملخص

تتناول هذه الأطروحة تأثير الديوتيريوم في التغيرات البنيوية والخصائص الحرارية في مركب التقاطع الدوراني$Fe(NCS)_2(PM-BiA)_2$، حيث يشير PM-BiA إلى البيريدين-2-ألدهيد و إلى 4-أمينوبيفينيل. في هذا البحث، تم استبدال الهيدروجين بـ 95.7% من الديوتيريوم في مركب 4-أمينوبيفينيل، ثم تم دمجه مع البيريدين-2-ألدهيد. تم تحضير البنيتين البلوريتين معينية الشكل و أحادية الميل بعد معالجتهما بالديوتيريوم بشكل جزئي مع ظهور بعض الشوائب و تمت مقارنتهما مع المركب البروتوني، وذلك باستخدام تقنيات حيود الأشعة السينية ونظام قياس الخواص الفيزيائية ، والتحليل الحراري التفاضلي .

يؤثر الديوتيريوم بشكل كبير على درجة حرارة الانتقال، مما يؤدي إلى انخفاض في البنية أحادية الميل وزيادة في المعينية القائمة عند مقارنتها بالمركب البروتوني. ويمكن أن يعزى هذا لنتيجة تأثير الديوتيريوم على خفض الطاقة اللازمة لانتقال الدوران وتغيرات في الكتلة المخفضة والتي تؤثر على اهتزازات الشبكة. علاوة على ذلك، فإن إشراك المواقع الديوتيريومية في الرابطة الهيدروجينية يزيد من درجة حرارة الانتقال.

بالإضافة إلى خصائص أخرى، تظهر بنية المعين القائم زيادة في جميع معلمات الشبكة، على عكس أحادي الميل. الذي يُظهر سلوكًا مختلفًا، مما قد يُشير إلى اختلاف الحجم أو الكثافة. أيضا، نتائج المحتوى الحراري والإنتروبيا أظهرت أن الديوتيريوم يؤدي إلى انخفاض كبير في القيم ويعزى ذلك إلى انخفاض طاقة النقطة الصفرية وضعف التآثر التعاوني في النظام.

تسلّط هذه النتائج الضوء على تأثير الاستبدال بالديوتيريوم على سلوك التحول الدوراني، كما تمهد الطريق للعمل المستقبلي من خلال تحضير مركبات معالجة بالكامل بالديوتيريوم وتحليل البلورات المفردة.

Table of Contents

List of Figures

List of Tables

List of Abbreviations

VCC	Vapor Compression Cycle
SCO	Spin Crossover
LS	Low spin
HS	High spin
PM	Pyridine-2-aldehyde
BiA	4-aminobiphenyl
$T_{1/2}$	Transition Temperature
LFT	Ligand Field Theory
CFT	Crystal Field Theory
MOT	Molecular Orbital Theory
CFSC	Crystal Field Splitting Energy
B	Racah parameter
γ_{HS}	High spin fraction
amu	atomic mass unit
ΔH	Enthalpy change
ΔS	Entropy change
Ω	The number of microstates
k_B	Boltzmann constant
χ	magnetic susceptibility
N_A	Avogadro number
DMSO	Dimethyl sulfoxide
DCM	Dichloromethane
PPMS	Physical Property Measurements System
ω	Frequency
Oe	Oersted
DSC	Differential scanning calorimetry
XRD	X-ray Diffraction

Chapter 1: Introduction

1.1   Motivation

Cooling systems play an important role in daily life and industrial processes, which rely on the vapor compression cycle (VCC) for 80% of all uses [1], and according to its environmental harm, such as global warming and ozone depletion, the urgent demand for environmentally friendly and energy-efficient technologies has arisen, hence cooling technologies have received a lot of attention in the 20th century's [2]. One of the most promising next-generation solutions is ferroic cooling technologies, which utilize caloric materials and are categorized based on the type of applied field.

Caloric effects, which are utilized to create a thermodynamic cooling cycle, involve a change in entropy or temperature when an external field is applied. [3]. Figure 1 depicts the caloric cooling cycle for barocaloric materials, which exhibit materials undergoing high-entropy change, reversible phase transitions, proper transition temperature, and low hysteresis in response to a small pressure change [4].

This objective can be achieved through the concept of phase transition occurring in spin crossover complex, which can be realized using various transition metal-based materials such as Fe(III) or (II) [5], Co(II) [6], Mn(II) [6], Ni(II) [7]. The typical spin-crossover compounds are octahedrally coordinated complexes of Fe [8], where Fe in a d^5 or d^6 electronic configurations can exist in either a low spin state (LS) or high spin state (HS), depending on the ligand field strength and the spin pairing energy P [8].

 For this study, Fe(NCS)$_2$(PM-BiA)$_2$ consists of the central metal ion Fe and is surrounded by three pairs of nitrogen atoms: the pyridyl methylene ligand (N-PM), the aminobiphenyl ligand (N-BiA), and the thiocyanate ligand (NCS). Furthermore, this complex can be found in two polymorphic forms; one crystallizes in an orthorhombic structure with a thermal transition temperature of 177 K with a 5 K hysteresis, while the other adopts a monoclinic structure with a transition temperature of 210 K and a narrow hysteresis of 1 K [9]. Such a difference renders it an ideal platform for investigation.
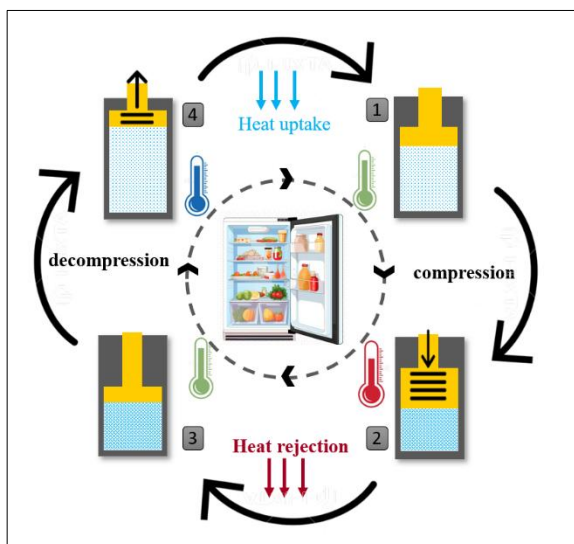
Figure 1: Illustration of Barocaloric refrigeration cycle, step (1-2): the material undergoes compression, resulting in a rise in temperature and rejecting the heat in step (2-3); following step (3-4), the Barocaloric material is decompressed and the temperature decrees, then the material absorbs heat and retrains to the initial state 1. Adapted from [4].

The first application of deuterium in spin crossover results in significant temperature shifts of 14 degrees in the spin conversion process, opening new avenues for optimizing barocaloric effect in Fe-spin crossover complex [10]. Deuteration causes the crystal lattice to expand and exerts negative pressures. Consequently, specific intermolecular

interactions are expected to change upon deuteration. Altering the strength and nature of these interactions and influencing the stability of the complex [10] is necessary to reduce the intense background from spin incoherent contributions from the H atoms [11].

Chapter 1 provides a comprehensive overview of previous research on $Fe(NCS)_2(PM-BiA)_2$. It delves into the fundamental aspects of the spin-crossover phenomenon, emphasizing the interplay between entropy, temperature, and pressure. Special attention is given to the influence of deuterium substitution and its role in modulating the spin transition behavior. Chapter 2 surveys the characterization techniques used in the study, including X-ray diffraction (XRD), the PPMS DynaCool system, and differential scanning calorimetry (DSC). Chapter 3 presents a detailed analysis of the experimental data, examining the structural, magnetic, and thermodynamic properties and their observed trends.

Finally, Chapter 4 concludes the study by summarizing the key findings and outlining potential directions for future research in the field of deuterated spin-crossover compounds.

1.2   Ligand Field Theory (LFT)

1.2.1   Background of Ligand Field Theory

Many theories have been developed to find discernible explanations for the bond nature between the central metal ion and the surrounding ligands. Among these, the earliest theory of bonding that was proposed is the crystal field theory (CFT) or electrostatic theory, which was developed by Bethe [12], and expanded by Van Vleck [13]. Another important approach is molecular orbital theory (MOT) and ligand field theory (LFT), which was also developed by van Vleck *et al.*[14]. These hypotheses explain the bonding, orbital arrangement, and other characteristics of coordination complexes. In general, the coordination complex has a formula of [ML_6] in which M refers to the central metal ion and L refers to the ligand surrounding the metal ion [15]. When the number of connected ligands is 6, the complex adopts an octahedral geometry. The CFT model assumed that the ligand is negatively charged; on the other hand, the metal is positively charged, and it shows the ligand affecting the central metal atom with an originating electric field influencing the arrangement of its d-orbitals without allowing mixing or overlapping of energy levels, by splitting the d-sublevel, between the axes, d_{xy}, $d_{xz,}$ and d_{yz}, and the d-sublevel, on the axes, d_{z^2} and $d_{x^2-y^2}$ (Figure 2-a) [16].
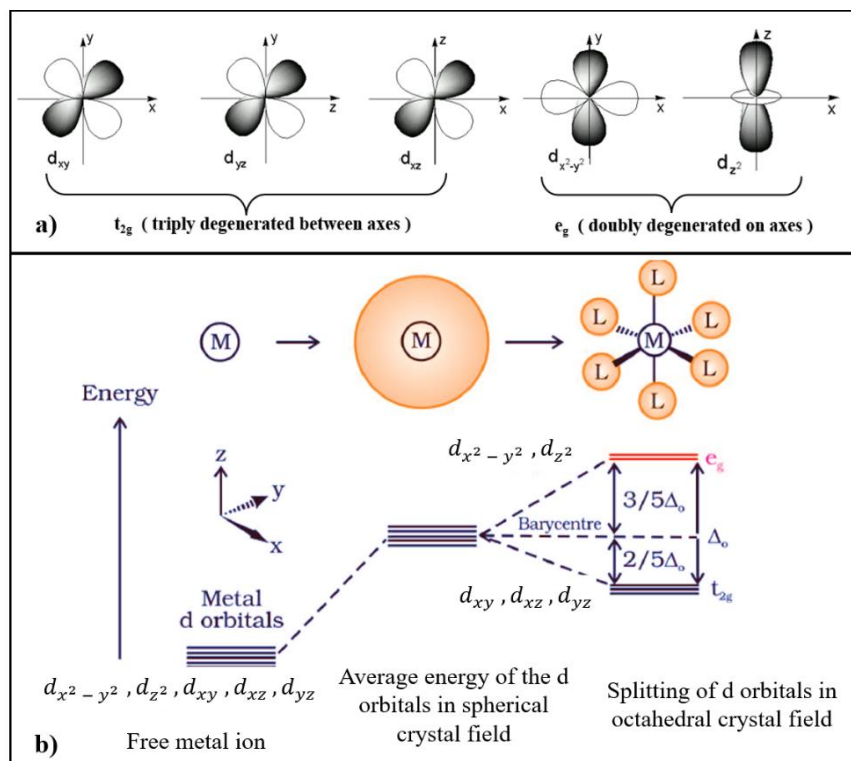
Figure 2: a) d sub-level orientations. Three are located between the axes (d_{xy}, d_{xz}, d_{yz}), and the other two are on the axes (d_{z^2}, $d_{x^2-y^2}$), b) crystal field splitting of 5d orbitals of the energy level, two separated groups were created, e_g (d_{z^2}, $d_{x^2-y^2}$) and t_{2g} (d_{xy}, d_{xz}, d_{yz}). Adapted from [16].

The complex contains a transition metal ion Fe (II), surrounded by 6 nitrogen atoms, forming an octahedral, the field generated by ligands causes uneven effects on d-orbitals. This asymmetry results in the splitting of degenerate d-orbitals, raising the energy of the e_g level for higher repulsion and decreasing the energy of t_{2g} level, with an energy gap called crystal field splitting energy (CFSE) indicated as Δ_o, Δ_{oct}, or 10Dq. The "$_o$" in Δ_o stands for octahedral. With 0.4 Δ_o for the three t_{2g} orbitals and 0.6 Δ_o for the two e_g orbitals. Figure 2-b illustrates this crystal field splitting in an octahedral coordination complex.

In many transition metals the electron configuration ended by $3d^n$, where n = 4~7, it can be distributed in two ways under the influence of the ligand field, and the spin pairing energy P, if the spin pairing energy P is less than the ligand field energy Δ_o (Δ_o >> P), the lower t_{2g} orbitals are occupied first and paring the electrons in t_{2g}, and create a low spin configuration. Conversely, if the spin pairing energy P is greater than the ligand field intensity Δ_o (Δ_o << P), the occupation of the orbitals is populated in such a way that there is a maximum total spin, for our transition metal in the selected complex. Fe^{+2} has an electronic configuration: $1s^2\ 2s^2\ 2p^6\ 3s^2\ 3p^6\ 3d^6$, the last 6 electrons can be in the high spin state ($^4t_{2g}$ - ^2e_g) with 4 unpaired electrons, so the total spin =2, which means a paramagnetic material, or in low spin state ($^6t_{2g}$ - ^0e_g) with no paring electrons and S=0, leading to a diamagnetic case [17]. Figure 3 illustrates the electron configuration of $3d^6$ in high spin and low spin for Fe(II).
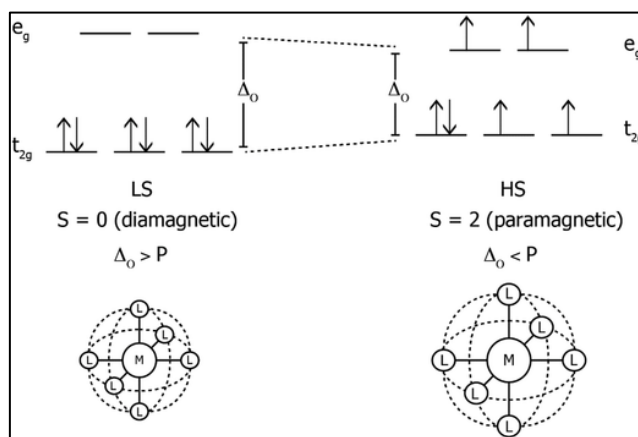
Figure 3: The electronic configurations of Fe(II) in an octahedral ligand field, showing the differences between low-spin (LS) and high-spin (HS) configurations. Taken from [17].

1.2.2   Factors Influencing Splitting Energy.

The d orbitals splitting energy can vary depending on several factors such as:

1- Oxidation state of the metal: The metal's capacity to draw electron density from ligands is improved by higher oxidation states, which usually result in stronger ligand fields because of increased positive charge. For example, comparing the Δ_o for $[Fe^{II}(H_2O)_6]^{+2}$ equals 10400 cm^{-1} and for $[Fe^{III}(H_2O)_6]^{+3}$ equals 13700 cm^{-1} [18].

2- Metal location in the periodic table: there are no significant differences across metals in the same transition series, while the Δ_o will differ significantly for metals in different columns. In particular, 4d and 5d metals generally adopt a low spin state because the splitting energy will be too large to handle the pairing energy of two electrons. As the transition moves from 3d to 4d to 5d, the splitting energy increases by approximately 25–50%. For example, the Δ_o in the hexamine complex $[M^{III}(NH_3)_6]^{+3}$, where M is the central ion. The Δ_o values are 22.870 cm^{-1} when M = Co (3d), 34.100 cm^{-1} for Rh (4d) and 41,200 cm^{-1} for Ir (5d) [18].

3- The presence of the ligands influences the distribution of the electrons within a coordination complex. Some ligands force the complex into either a high spin state or low spin state. This behavior depends on the spectrochemical series, which is an empirical arrangement of ligands based on their ability to split the d-orbitals of a central metal ion in a coordination complex. If the ligand field is

weak, as iodide (I⁻) and bromide (Br⁻), the splitting energy is smaller, so this helps in creating the high spin state. In contrast, if the field is strong as cyanide (CN⁻) and carbon monoxide (CO), it will create a larger splitting energy that exceeds the pairing energy, which forces the electrons to pair within t_{2g} orbitals before occupying the e_g orbitals, resulting in a low spin state. Ligands can be organized in a series depending on their field [19] as follows:

Small Δ_o, High spin, weak field: $I^- < Br^- < S^{-2} < Cl^- < OH^- < RCO^-_2 < F^- < H_2O < NCS^- < NH_3 < NO_2^- < Phen < CN^- < CO$: large Δ_o, Low spin, strong field.

1.3   Spin Crossover (SCO)

1.3.1   Principle of Spin Crossover

The discovery of spin crossover (SCO) originated with Cambi and co-workers in the 1930s, when they observed Iron(III) derivatives of various dithiocarbamates undergoing interconversion of two spin states as a result of variation in temperature [20]. Then the first recognition of this phenomenon, which expanded by Baker and Bobonich who reported the magnetic moments of the series of compounds cis-[FeX$_2$(phen)$_2$] (phen = 1,10-phenanthroline; Where X⁻ = Cl⁻, Br⁻, I⁻ or N$_3$⁻ and observed a different behavior and unexpected magnetic momentum changes, particularly when X⁻ = NCS⁻(at 180 K) or NCSe⁻ (at 230 K) [21]. Later, an alternate theory put out by König and Madeja suggested that [Fe(NCS)$_2$(phen)$_2$] and

[Fe(NCSe)$_2$(phen)$_2$] were going through a thermal transition from their diamagnetic low-spin (S = 0) to paramagnetic high-spin (S = 2) states [22]. This made the [Fe(phen)$_2$(NCS)$_2$] become the first synthetic system in which spin crossover was shown to explain this unusual magnetic behavior [22]. Followed by enormous and continuous research due to significant attention, leading to extensive and ongoing research that remains highly relevant today.

Spin crossover, in other words, refers to a spin transition or spin equilibrium. It describes the transition between a low spin state and a high spin state due to an external stimulus like temperature, pressure, electricity, and light. This phenomenon can be found in the d^4-d^7 electron configuration of transition metal complexes with an octahedral ligand [8]. This feature makes it eligible for play with many potential applications, like sensors [23], memory devices, and smart materials [24].

1.3.2   Spin Transition Behavior

The nature of spin transition for any spin crossover complex can be described through a curve connecting the molar fraction of high spin called γ_{HS} versus temperature or pressure. There are 5 different transition forms illustrated in Figure 4 [25].

- Gradual Spin Transition (or continuous transition 4-a) refers to a smooth transition between high-spin (HS) and low-spin (LS) states. The transition can occur over a wide range of temperatures or pressures, as seen in a trinuclear iron complex, where the spin crossover was observed at 148 K due to weak

interactions between the molecules undergoing the spin transition [26]. Hence, each molecule's transitions are relatively independent [8]. This mainly takes place in a solution or a solid state [27]. It is widely used for developing materials for applications in molecular switches and information storage [28].
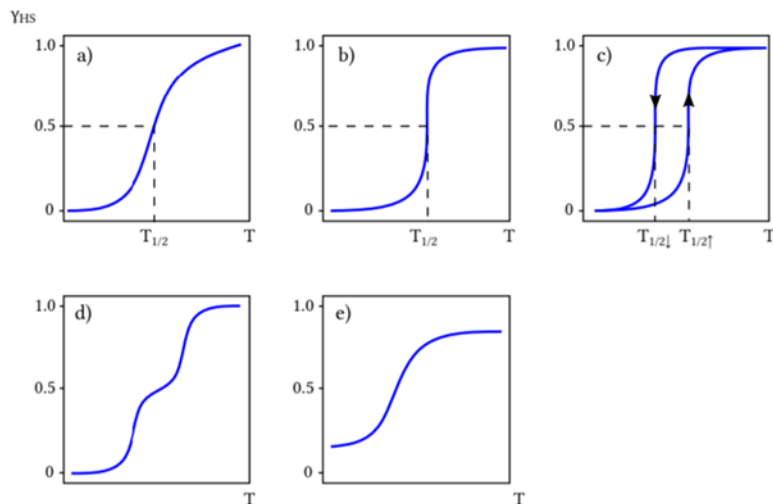
Figure 4: Curves for the spin phase transition show the high spin fraction as a function of temperature, (a) gradual, (b) abrupt, (c) Hysteretic, (d) two-step, (e) incomplete. $T_{1/2}$ is the temperature for which there is a coexistence of 50% of LS and 50% of HS molecules.

- Abrupt Spin Transition: (Figure 4b) refers to a sudden change in the spin state of a material, typically accompanied by a certain temperature or pressure threshold [8]. The Fe(II) complex undergoes an abrupt spin transition at 127 K with a narrow thermal hysteresis, indicating a sharp change from HS to LS states [29]. This occurs due to strong cooperative interactions, meaning that a change in one molecule's spin state influences its neighbors, leading to a coincident switch [30]. It can be used as a study case for the barocaloric effect as $[Co^{II}(dpzca)_2]$, which shows a quick change from HS to low-spin LS states

[31]. $Fe(NCS)_2(PM-BiA)_2$ also shows two phase transitions that would be fit for a barocaloric effect [9].

- Hysteretic Spin Transition: (Figure 4c) refers to the phenomenon where spin-crossover (SCO) materials display different HS and LS states at specific temperatures; in other words, when moving from LS to HS or vice versa, each step happens at different temperatures or pressures, one for decreasing $(T_{1/2}\downarrow)$, and one for increasing temperature $(T_{1/2}\uparrow)$, resulting in a thermal hysteresis loop [8]. This could happen according to the structural phase change or due to strong communication in a highly cooperative system through the intramolecular structural changes [9]. These LS and HS transitions enable bistability, which allows them to be used as memory devices [25].

- Two-Step Spin Transition: (Figure 4d) happens when the material exhibits two different stages between HS and LS states. The first stage may include a partial LS to HS transition, followed by a second step at a different temperature or pressure, in which the remaining centers flip [8]. This behavior can arise from the binuclear systems [32], short-range interactions, and the preferential formation of HS/LS pairs in the progress of the transition at a single lattice site [33].

- Incomplete Spin Transition: (Figure 4e) It shows a complex that cannot reach a fully HS or LS state. A residual γ_{HS} will be observed even at low temperatures.

This reflects an incomplete spin crossover due to lattice defects, misalignments, or even impurities in the sample [30].

1.4 Fe(NCS)$_2$(PM-BiA)$_2$

Fe(NCS)$_2$(PM-BiA)$_2$ (FeS$_2$N$_6$C$_{38}$H$_{28}$) is widely utilized in investigating the SCO phenomenon. It is a mononuclear iron(II) complex, where PM-BiA stands for N-(2-pyridylmethylene)-4-Aminobiphenyl. As shown in Figure 5, its molecular structure consists of a central Fe^{2+} ion coordinated octahedrally by four nitrogen atoms from two bidentate PM-BiA ligands and two nitrogen atoms from terminal thiocyanate (NCS$^-$) ligands. Each PM-BiA ligand forms a five-membered chelate ring via its imine nitrogen and pyridyl nitrogen donor atoms. The thiocyanate ligands occupy the axial positions, completing the octahedral coordination sphere.
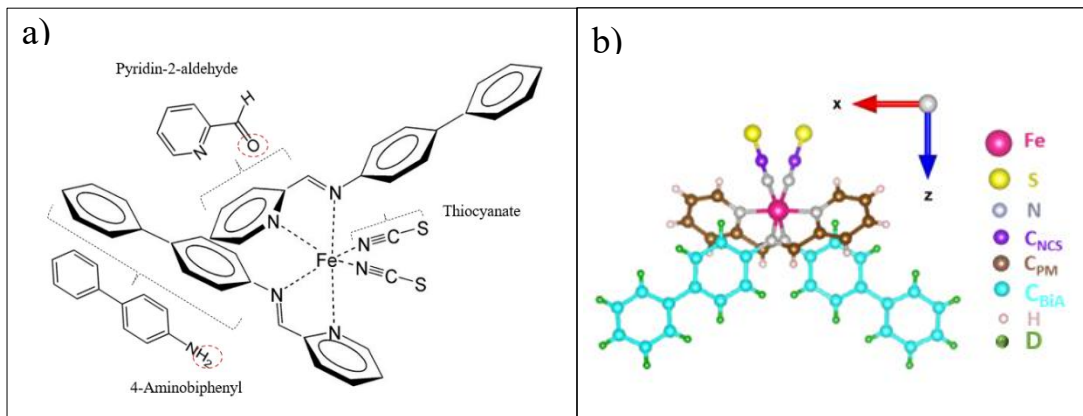
Figure 5: Scheme of the [Fe(NCS)$_2$(PM-BiA)$_2$] complex, with an explanation of each component: thiocyanate (NCS)-, 4-aminobiphenyl (BiA), 2-pyridine methanol (PM), the two dashed circle O from pyridine-2-aldehyde and H$_2$ from 4-aminobiphenyl released from this complex as a water molecule. a) schematic molecular representation. b) Crystallographic representation with unit cell orientation

This complex has two different polymorphs, orthorhombic with space group *Pccn* (phase I) and monoclinic with space group *P2₁/c* (phase II). These two polymorphs exhibit different spin transitions, where the orthorhombic polymorph shows an abrupt transition with $T_{1/2\uparrow}$=173 K and $T_{1/2\downarrow}$= 167 K with a 6 K hysteresis loop, and the second is a gradual transition at nearly 210 K with a range of 150-250 K [9] that is consistent with previous research results shown in Table 1.

Type of polymorphs	Nature of spin transition	Phase transition temperature	Reference
orthorhombic	Abrupt with small hysteresis	$T_{1/2\uparrow}$=173K $T_{1/2\downarrow}$= 168K with a 5K hysteresis loop	[34]
orthorhombic	Abrupt with small hysteresis	$T_{1/2\uparrow}$=173K $T_{1/2\downarrow}$= 167K with a 6K hysteresis loop	[9]
monoclinic	Gradual	$T_{1/2\uparrow}$=198K	[34]
monoclinic	Gradual	$T_{1/2\uparrow}$=210K	[9]

Table 1: Data collected from [9] and [34], for the transition temperature between the two polymorphs.
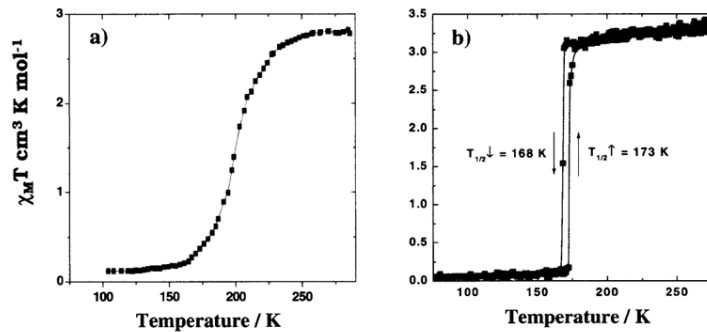
Figure 6: The magnetization curves for both phases from [34], a) monoclinic b) orthorhombic, the curves show the behavior depending on $\chi_M T$ product vs. T, where χ_M stands for the molar magnetic susceptibility.

Additionally, these two polymorphs exhibit different lattice parameters in their LS and HS states, which can vary with partially deuterated complexes. These parameters are illustrated in Table 2 for protonated complexes in both space groups.

Besides these features, some caloric properties have been studied as the entropy change for both monoclinic and orthorhombic, which is equal to (48 J mol^{-1}K^{-1}) [9] and (58 J mol^{-1}K^{-1}) [35], respectively. In addition, other features were revealed through Sandeman's calculation and Shahed's Experiments [9], motivating further investigations to explore this complex ability to exhibit barocaloric effects.

	Pccn [35]		*P2₁/c* [36]	
	Low spin	*High spin*	*Low spin*	*High spin*
a (Å)	12.370(3)	12.949(7)	17.362(1)	17.570(5)
b (Å)	14.764(3)	15.183(2)	12.302(1)	12.602(5)
c (Å)	18.281(4)	17.609(5)	17.050(1)	17.358(5)
β (°)	90	90	115.83(1)	115.68(1)
V (Å³)	3339(2)	3462(2)	3294(1)	3464(2)

Table 2: Lattice parameter for orthorhombic and monoclinic polymorphs of protonated Fe(NCS)₂(PM-BiA)₂.

1.5   Deuteration Effect

Deuteration, which involves substituting hydrogen atoms with deuterium, a stable isotope of hydrogen characterized by the presence of one proton and one neutron, has been shown to significantly impact the physical and chemical properties of molecular systems. In the context of spin-crossover (SCO) compounds, deuteration plays a vital

role in studying structural and macroscopic properties such as magnetic and thermodynamic effects, arising from varying the degree of deuteration in the compounds. It is also relevant for understanding the fundamental behavior of SCO materials and optimizing their performance in technological applications such as ferroic cooling.

1.5.1   The Role of Deuteration

In principle, substituting deuterium in ligands or lattice components influences chemical bonds such as C-D and N-D in $Fe(NCS)_2(PM-BiA)_2$, which would lower their vibrational frequency [37]. Also, it enhances isotope stability due to the stronger N-D [38].

The primary advantage of using deuterium lies in its suitability for investigating and studying such complexes via neutron scattering. The significant difference in incoherent scattering cross sections between H (σ_{inc} =80.27×10^{-28} m^2) and D (σ_{inc} =2.05×10^{-28} m^2)   provides valuable insights into the atomic structure and behavior of hydrogen and deuterium in various materials [39]. This thesis focuses on the macroscopic effects of deuteration, including structural modifications, such as changes in atomic bonding and thermodynamic properties related to the spin transition, specifically the transition temperature, enthalpy change (ΔH), and entropy change (ΔS). In addition, it explores the magnetic properties associated with the transition

between low-spin (LS) and high-spin (HS) states, which results in a change in the magnetic moment.

1.5.2 Deuteration Effect on Spin Crossover

The SCO phenomenon involves a transition between HS and LS, which can be significantly influenced by deuteration. In SCO complexes, using deuterium can be regarded as introducing negative pressure through the complex [40]. One of the key effects of deuteration in spin-crossover (SCO) systems is the shift in transition temperature, attributed to reduced vibrational energy and shortened bond lengths that stabilize the low-spin (LS) state. As the [Fe(5-NO$_2$-sal-N(1,4,7,10))] SCO complex was evaluated within the H/D isotope effect, it raised the critical temperatures (T$_{c1}$ from 140.5 to 150.3 K, T$_{c2}$ from 176.8 to 183 K). The cooperativity of the spin-state transition is preserved, but can be modulated by changes in hydrogen bond lengths, which slightly weaken these interactions and may lead to an increase in the ligand field strength, thereby raising the transition temperature T$_{\frac{1}{2}}$ [41], it can be interpreted from the energy point of view $\Delta E = E_{HS}^0 - E_{LS}^0 = \frac{1}{2}hcv_{HS}^0 - \frac{1}{2}hcv_{LS}^0$, where v^0 is the wavenumber of the zero-point vibrations, and is equal to: $v = \frac{1}{2\pi c}\sqrt{\frac{k}{\mu}}$, where k is the effective force constant and μ is the reduced mass. Once, $\frac{1}{\mu_D} < \frac{1}{\mu_H}$ and $k_{HS} < k_{LS}$ in the deuterium and protonated case [42], so the difference of energy is represented as $\delta(\Delta E) = \Delta E(D) - \Delta E(H)$ while it is positive, it implies that the relative stability of

the LS state increases and thus the transition temperature $T_{1/2}$ shifts upwards upon deuteration [10].
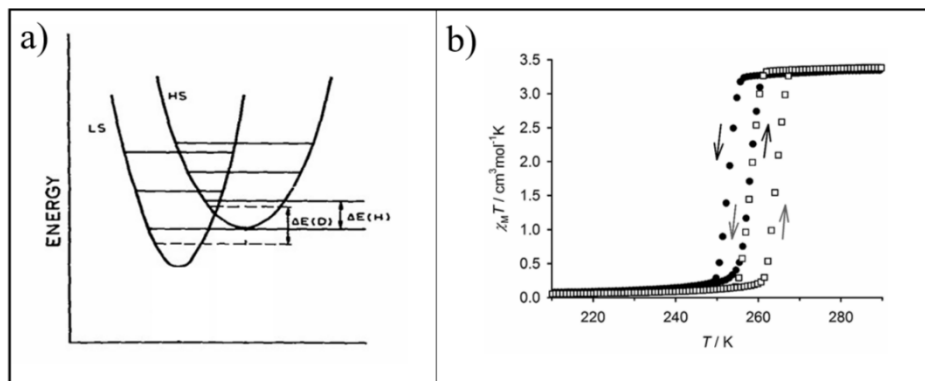
Figure 7: a) Schematic vibronic energy level diagram for a d6 Ion in the LS state and the HS state. Taken from [10]. b) The partial deuterated effect of [FeL$_2$][BF$_4$]$_2$ complex on the spin transition curve, the empty square for the protonated one, and the solid circle for the partial deuterated sample. Taken from [44].

The entropy change can also be modulated with deuteration, where the lattice vibration is involved. In other words, vibrational modes in the HS state are considerably softened, reducing the entropy gain upon HS transition. This favors LS at lower temperatures and decreases $T_{1/2}$, as this study, a protonated and partially deuterated polycrystalline [FeL$_2$][BF$_4$]^2 [L = 2,6-di(pyrazol-1-yl)pyridine] are shown to exhibit a change in both transition temperature and entropy. Figure 7b shows the shift in transition temperature for the protonated and partially deuterated sample to be (T $_{(1/2\uparrow)}$ = 262 K; T $_{(1/2\downarrow)}$ = 258 K); (T $_{(1/2\uparrow)}$ = 257 and T $_{(1/2\downarrow)}$ = 253 K), respectively. The hysteresis loop width of 4 K is seen for both cases [43]. while the entropy change of the protonated compound ΔS_H (66.2 J mol^{-1} K^{-1}) [44] is slightly larger than ΔS_D (56 J mol^{-1} K^{-1}) in the deuterated compound [43].

1.6 Physical Properties

1.6.1 Thermodynamic Properties

This section establishes the characterization of the spin transition, driven by changes in thermodynamic parameters. According to the first principle in thermodynamics [45]:

$$dU = \delta Q - \delta W \tag{1.1}$$

Where U refers to the internal energy of the system, Q refers to the system's heat, and W refers to the work, written as the product $P \times \Delta V$. And the heat added to a system is proportional to the temperature and the corresponding change in entropy [45]:

$$\delta Q = T\, dS \tag{1.2}$$

So, the whole equation 1.1 becomes equation 1.3, which shows the dependence of U on S and V, in other words U it is a function of S and V, $U = U(S, V)$

$$dU = T\, dS - P\, dV \tag{1.3}$$

Another quantity called enthalpy is represented as a function of entropy and pressure [46], which is equal:

$$H = U + PV = TS \tag{1.4}$$

The spin crossover transition from HS to LS relies on the amount of entropy changes ΔS, which can be written as (1.5) [47]:

$$\Delta S = S_{HS} - S_{LS} = k_B \ln(\Omega_{HS}) - k_B \ln(\Omega_{LS}) = k_B \ln\left(\frac{\Omega_{HS}}{\Omega_{LS}}\right) \qquad (1.5)$$

The total entropy in SCO compounds is contributed by four terms [48], electronic (S_{ele}), vibrational (S_{vib}), rotational (S_{rot}), and configurational(S_{con}). S_{rot} and S_{con}, can be neglected since the configurational entropy remains constant due to fixed metals and ligand positions, and rotational degrees of freedom in solid-state material are relatively restricted (i.e., $\Delta S_{con} = 0$ and $\Delta S_{rot} = 0$) [48]. Hence, the electronic and vibrational entropy contribute the most to the total entropy change.

The electronic term can be derived from both spin and orbital degeneracy; the orbital effect is removed, so the electronic entropy is caused by the spin participation, as follows:

$$\Delta S_{ele} = R \ln\left(\frac{2S_{HS} + 1}{2S_{LS} + 1}\right) \qquad (1.6)$$

Where R is the gas constant, which is equal to the multiplied of the Boltzmann constant with Avogadro's number, R =$K_B.NA$= $1.38 \times 10^{-23} \times 6.022 \times 10^{23}$ = 3.316 J mol^{-1}K^{-1}, for example, the Fe-SCO complexes, the $\Delta S_{ele} = R \ln(5) = 13.38$ J mol^{-1}K^{-1} [49], where S_{HS}=2 and S_{LS}=0.

The vibrational entropy, which occurs from the variation in the metal-ligand distances, resulting from stretching and deformation oscillations, can be written through equation (1.7):

$$S_{i\,.vib} = \frac{hv}{2k_BT}\tanh\left(\frac{hv}{2k_BT}\right) - k_B\ln\left(2\sinh\left(\frac{hv}{2k_BT}\right)\right) \tag{1.7}$$

So, the vibrational entropy changes related to the spin transition can be obtained to be:

$$\Delta S_{i,vib} = S_{i\,.vib}(v_{HS}, \text{T}_c) - S_{i\,.vib}(v_{lS}, \text{T}_c) \tag{1.8}$$

This explains the discrepancy in entropy change, which exceeds the contribution from electronic entropy alone, resulting in a range of 68–85 J mol^{-1}K^{-1} for Fe-based SCO complexes. [48] and [50]. Note that entropy change can be experimentally evaluated using calorimetric techniques, such as differential scanning calorimetry (DSC), or calculated from the transition temperature ($T_{1/2}$) and enthalpy change (ΔH): $\Delta S=H\backslash T_{1/2}$.

The most essential consideration in determining whether a material is suitable for caloric materials through the nature of the phase transition [51] [52] which can be sharp (1st order) or gradual (2nd order). In the spin crossover phenomenon, at equilibrium, ΔG=0, ΔH = TΔS. This occurs at the temperature (T$_{1/2}$) when half of the molecules are in the HS state and the rest are in the LS state.

1.6.2 Magnetic Properties

Understanding the magnetization for the spin crossover reveals the population of LS and HS states as a function of external stimuli such as temperature or pressure. The total spin for 3d electrons in the Fe (II) complex in LS equals zero (S = 0), resulting from the 6 paired electrons. For HS, the total spin can be measured by $S = \frac{1}{2}$ (no. of

spin up − no. of spin down) = $\frac{1}{2}$ (5 -1) = 2. Figure 3 represents the magnetic moment

for each state. In the spin crossover compounds, the complex behaves as a

paramagnetic or diamagnetic material when it is in the HS or LS state, respectively.

To distinguish between these two materials, the magnetic susceptibility (χ) is measured

to determine the magnetization (M) generated in the material. If $10^{-5} < \chi < 10^{-3}$, the

material is paramagnetic, whereas if $\chi < 0$, the material is diamagnetic [53].

Importantly, χ of diamagnetic materials is temperature independent because of no free

electrons available in this type of material. Conversely, χ of paramagnetic materials

varies inversely with temperature (i.e., $\chi = C/T$, where C is the Curie constant) [54],

[55].
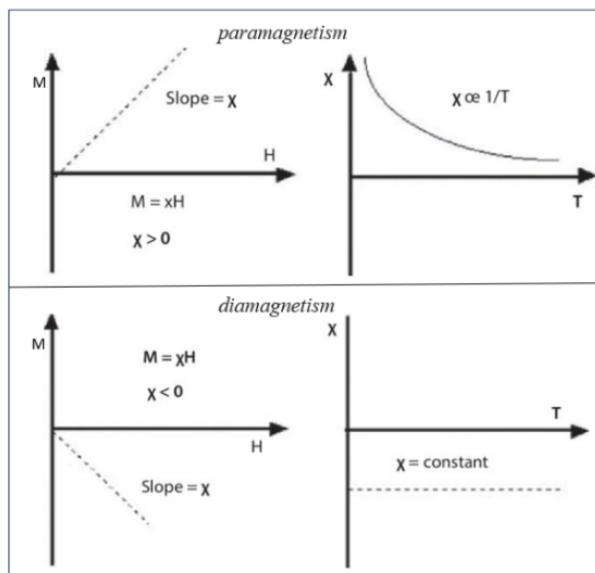
Figure 8: Magnetic susceptibility vs. temperature, for both paramagnetism and diamagnetism [55].

Chapter 2: Characterization Technique and Instruments

2.1 X-Ray Diffraction (XRD)

2.1.1 In-house XRD Measurements

X-ray diffraction is widely used to identify the structure of each two polymorphs and detect the impurity of the observed profile. The instrument used to figure out this information is the Huber diffractometer with Cu-Kα X-ray source ($\lambda = 1.5406$ Å) with the G670 Guinier Camera mounted on the Huber Diffractometer.
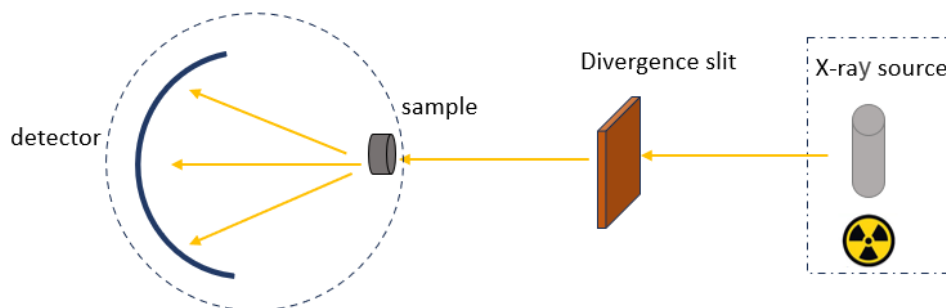
Figure 9: Schematic Diagram of the X-ray Diffraction (XRD) Setup

Figure 9 illustrates the basic components of an X-ray diffraction system. The incoming monochromatic X-ray beam from the X-ray tube interacts with the sample, which is prepared as a thin layer of powder between two plastic films. A divergence slit, located between the X-ray tube and the sample, ensures a controlled beam path. The diffracted beams are then detected at various angles by the detector.

The recorded data will be presented in X-ray pattern, where refinement and analysis with JANA 2006 software [56], in terms of scattered intensity vs. angle of diffraction.
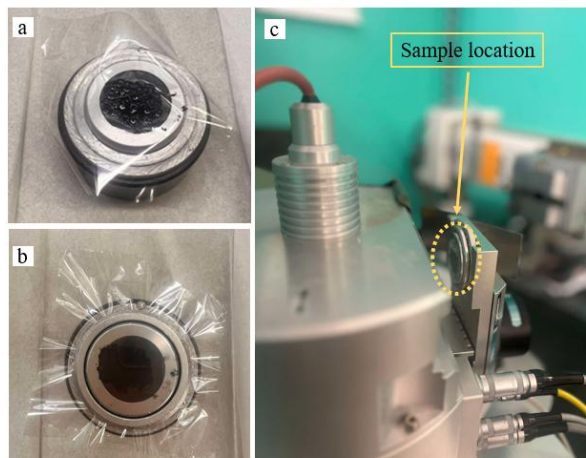
Figure 10: a) Prepare the sample, first putting a slice of transparent paper fitting the metal circle, adding a few amounts of the sample in the middle, applying 2 drops of isopropanol, letting it to dry, then covering it by another layer of transparent paper, close it carefully like(b) then adjust it vertically as shown in (c).

2.1.2 Synchrotron XRD Measurements

The synchrotron XRD experiment is held in Beamline P08, which resides at the 3rd generation synchrotron radiation source PETRA III in Hamburg, Germany. It is designed for high-resolution diffraction and scattering studies of condensed matter samples. In diffraction geometry, crystal lattice parameters can be determined with an accuracy of 10-5, whereas in small-angle scattering. The photon energy can be tuned between 5.4 and 29.4 keV with a flux of 1011 to 1012 photons per second (any further info can be found easily on the DESY website). For this experiment, the measurement was done for both monoclinic and orthorhombic samples at room temperature with 25 keV, which equals 0.4959Å, with 2θ from 0º to 40º, the collected data containing 2

columns, the first for the q which represent the scattering vector vs. intensity, so to draw the XRD pattern, the q values must convert to 2θ following this relation:

$$q = \frac{4\pi}{\lambda}\sin(\theta) \dots so, 2\theta = 2 \times \sin^{-1}\left(\frac{q\,\lambda}{4\,\pi}\right) \tag{2.1}$$

And convert it from radians to degrees by multiplying it by the factor 57.2958 degrees/rad. Then the new data would be 2 columns for 2θ vs. intensity
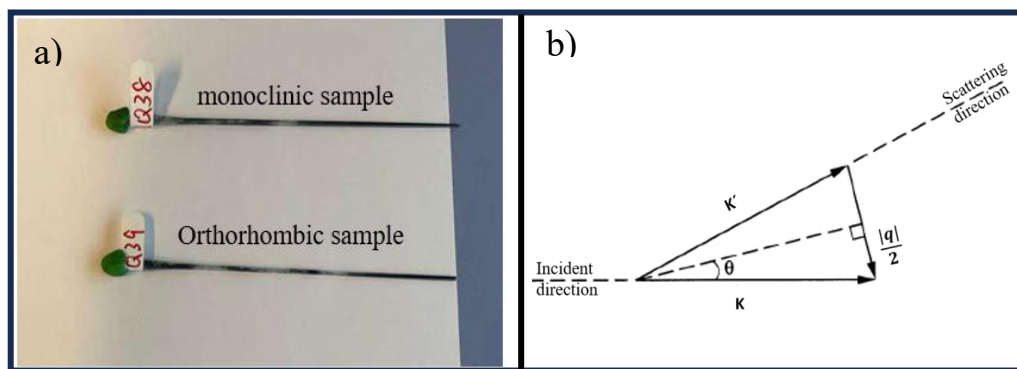
Figure 11: a) sample for the P08 beamline by a capillary covered by clay. b) Schematic Representation of the Scattering Vector in Reciprocal Space.

This relation comes from the incident and scattered wave vectors as shown in Figure 11-b. [57]. For the sample preparation, a capillary was filled with the sample carefully and closed with a piece of clay, with the name of the sample as shown in Figure 11-a.

2.1.3 Le Bail refinement

Regarding the determination of structural properties, the Le Bail refinement, introduced by Armel Le Bail in 1988 [58], was applied to powder diffraction data. This method is used for fitting profiles of entire diffraction patterns that are used to describe the structure.

The Le Bail refinement depends basically on the Least squares approximation, employing an iterative process that adjusts parameters based on Bragg's law, by refining these parameters to ensure an optimal match between the calculated and observed diffraction profiles.

A software program can be used to refine X-ray diffraction (XRD) data. In this case, JANA 2006 was used, incorporating lattice parameters from the literature, which were obtained from single-crystal XRD data. Additionally, the space group was specified during the refinement process.

The refinement processes primarily rely on knowing the Bragg relation; in this study, the X-ray wavelength is fixed and cannot be refined. Therefore, the two adjustable parameters are the scattering angle θ and the interplanar spacing d, depending basically on the lattice parameters (a, b, c), and the angles (α, β, γ). Start fitting by setting the background subtraction, where a manual background is created using 30–40 points. The profile function is selected as a pseudo-Voigt function, which combines Lorentzian and Gaussian components. The profile is then adjusted to achieve an optimal fit before refining the zero shift, which may arise due to sample positioning errors or instrument misalignment. Further steps can be done depending on the software itself, regarding some modifications for fitting the profile.

2.2 Physical Properties Measurement Systems (PPMS) DynaCool

2.2.1 PPMS DynaCool Measurements

The Physical Property Measurement System (PPMS) dynacool is a versatile, fully integrated instrument designed for the measurement of a wide range of physical properties of materials under precisely controlled conditions. It is widely used in condensed matter physics and materials science research for characterizing superconductors, magnetic materials, and correlated electron system. Using vibrating sample magnetometer (VSM), the magnetic moment of a sample can be measured with a sensitivity down 10^{-6} emu, The sample vibrates in a magnetic field generated by superconducting solenoid magnets, allowing fields up to ± 9 T to be applied, to induce vibrations on a sample, a linear transport motor is used, the sample surrounded by pickup coils to detect its magnetic response, the output of the pickup coils is connected to an amplifier [59].

The working principle of this device is based on Faraday's Law of Induction, via relation represents the induced voltage in the pickup coil and the time derivative of the magnetic flux, which is also proportional to many parameters illustrated in equation (2.2), as the amplitude of the oscillation (A), the frequency (ω), the coupling constant C and the magnetic moment of the sample(m).

$$V_{coil} = \frac{d\emptyset}{dt} = A \, \omega \, C \, m \sin(\omega t) \qquad (2.2)$$

The device is equipped with a temperature controller, allowing the sample temperature to be set between 1.8 and 400 K. The device setup can be presented in Figure 12.

For the procedure, we install the VSM option by making sure the sample chamber is below room temperature and the magnetic field is set to 0 Oe. regarding the preparation of the sample, each sample has been weighted to be 8 milligrams for both monoclinic and orthorhombic complexes, filled in a plastic capsule, and placed in the brass tube, considering the sample parallel to the center at 35 mm see Figure 12. This step guarantees that the centering of the oscillation will be in the pickup coil region.
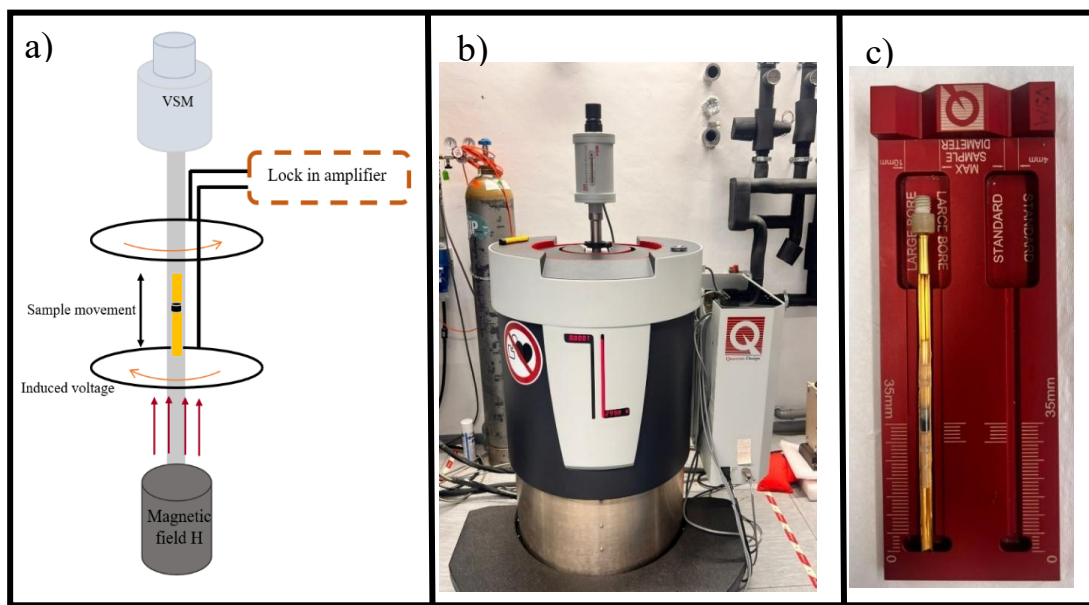
Figure 12: a) The schematic shows the principle of VSM DynaCool by vibrating through the magnetic field and detecting induced electromagnetic force through the pickup coils. b) PPMS dynaCool device. c) Sample prepared by putting the sample (the dark powder) inside a plastic capsule, and centering it in the brass tube.

This technique had been used to collect the response of the magnetic field as a function of the temperature by fixing the generated magnetic field (H) at 500 Oe = 0.05 T. These measurements were carried out at different scan rates (1, 2, 5, 10, and 20 K/min) for cooling and heating modes from 5-350 K.

2.2.2   Correction of PPMS DynaCool Data

The raw data were corrected by relating the paramagnetic and diamagnetic contributions since the total magnetic susceptibility is a summation of two terms from diamagnetic and paramagnetic susceptibility [60]. The correction depends on understanding the Curie law that describes the temperature dependence of the magnetic susceptibility (χ) in paramagnetic materials, which is given by:

$$\chi = \frac{C}{T} \tag{2.3}$$

In systems with low-temperature paramagnetic impurities, the raw magnetization data measured from a PPMS setup contain contributions not only from the intrinsic magnetic moments of the sample but also from extrinsic sources, such as diamagnetic background from the sample holder. This required a correction concerning both paramagnetic and diamagnetic noise, by applying this equation:

$$M_{correct} = M_{raw} - \left(\frac{\alpha}{T} + \beta\right) \tag{2.4}$$

In this equation, the constant α represents the paramagnetic (temperature-dependent) contribution of impurities, which could arise due to residual unpaired spins that do not interact strongly with the primary system and follow simple Curie behavior. And the additional correction term, β corresponds to temperature-independent diamagnetic.

By obtaining these factors, the magnetic momentum can be fitted in two regions first region with a temperature range from 5-100 K and the second region with 225-350 K,

which can be shown in Figure 13, for the molar magnetic susceptibility is multiplied by temperature through this equation (2.5) after correction, and the HS fraction calculated through equation (2.6).

$$x_M.\mathrm{T} = \frac{M\left[\frac{cm^3}{oersted}\right] \times MolarMass\left[\frac{gram}{mol}\right]}{H[oersted] \times mass\,[gram]} . \text{Tempreure}\,[Kelvein] \qquad (2.5)$$

$$\gamma_{HS} = \frac{x_M(LS) - x_M.T(T)}{x_M(LS) - x_M.T(\mathrm{HS})} \qquad (2.6)$$
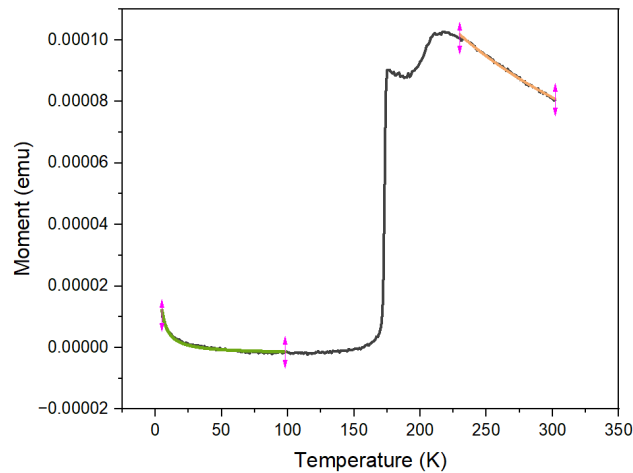
Figure 13: The raw data indicated by the black curve, and the two regions (orange and green) applying the fitting equation to extract the parameter for making corrections and getting some-how pure data.

2.3 Differential scanning calorimetry (DSC) measurements

Differential Scanning Calorimetry (DSC) measures the heat flow difference between a sample and a reference as a function of temperature or time to detect phase transitions and thermal events based on enthalpy changes. In spin crossover compounds, the

material will exhibit a change from LS to HS, which provides an endothermic process, and upon transforming inversion from HS to LS, the process will be exothermic [61], as can be shown in Figure 14.
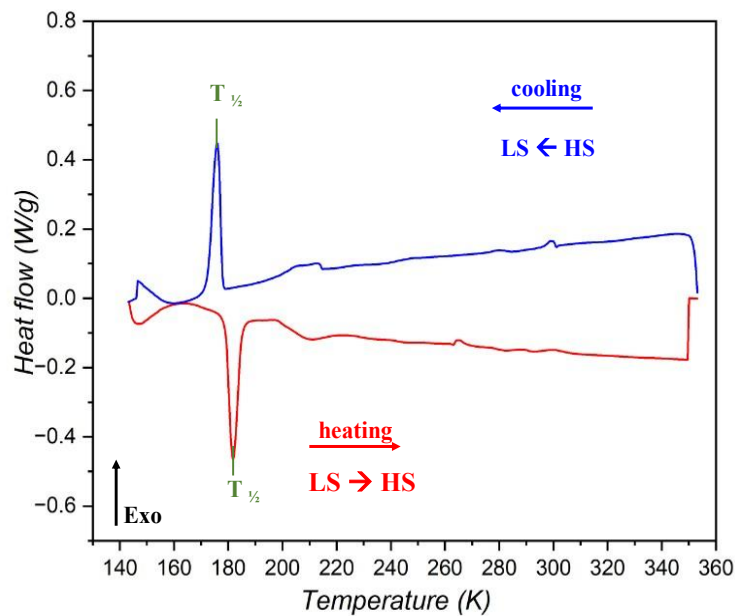
Figure 14: Experimental curves for a Differential Scanning Calorimetry analysis (DSC) for the spin crossover material. the flow of heat is measured. The responses seen here are transition temperature, exothermic cooling, and endothermic heating.

The Perkin Elmer Pyris Diamond DSC-2000 calorimeter was installed in the measurement setup. The heat flow difference required to heat a sample, which is nearly a few milligrams of polycrystalline material, and a reference pan made of aluminum material, and to close the sample pan with its lid, a capsule press is used to press the contents homogeneously, then the two pans are placed in separate heating chambers and measure the difference in heating flow. The setup parts are shown in Figure 15.
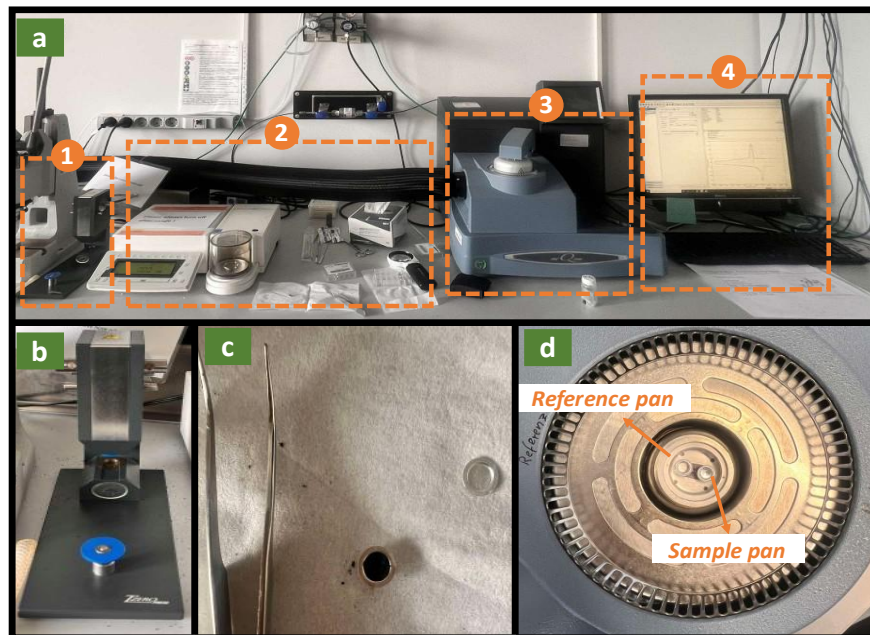
Figure 15: The DSC device used during the experiment. (a) Shows the entire setup, highlighting four regions: 1. The compression press, clearly visible in photo (b), where the sample is placed in its holder and compressed manually.2. The sample preparation area, where several steps are followed: weighing the empty pan and lid, filling the pan with the sample, sealing it, and then recording the total mass of the sample, pan, and lid, photo (b) shows the size of the pan. 3. The chamber contains two disc-shaped platforms for placing the sample and reference, as shown in photo (d). 4. The measurement display screen, which runs the TA Universal Analysis software.

The DSC is equipped with liquid nitrogen cooling and could be cooled down to approximately -170°C; the upper limit of the temperature range is 600°C, with different scanning rates of between 0.01 and 500°C/min. However, typical scanning rates range from 5 to 40 °C/min. Generally, slower scanning rates improve the peak resolution, while faster scanning rates improve sensitivity.

Chapter 3: Results and Discussion

3.1   Sample Preparation

3.1.1   Deuteration of 4-aminobiphenyl (BiA)

To confirm the effectiveness of the deuteration process, ^{1}HNMR spectroscopy was conducted on the deuterated 4-aminobiphenyl ligand. The obtained spectrum, shown in Figure 16, reveals distinct peaks corresponding to different molecular components in the sample. The peak at (1) corresponds to the protonated BiA fragment. This signal serves as a reference to evaluate the degree of deuteration if it is compared with protonated BiA, as shown in Figure 17, as proton sites are exchanged by deuteration, resulting in the complete disappearance of this peak. The 3rd peak indicates ethyl carbonate, which is a stabilizer in the sample.
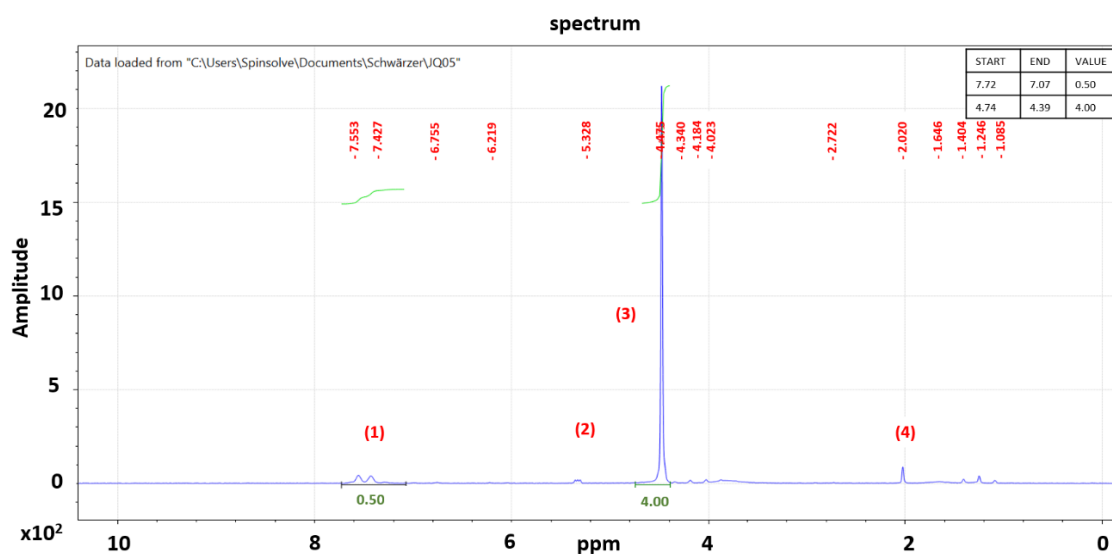
Figure 16: ^{1}HNMR analysis for the deuterated 4-aminobiphenyl.

The other peaks represent the residual solvent, as peaks (2) and (4) correspond to dichloromethane (DCM) and ethyl acetate, respectively, and they do not interfere with the analysis of deuteration efficiency.
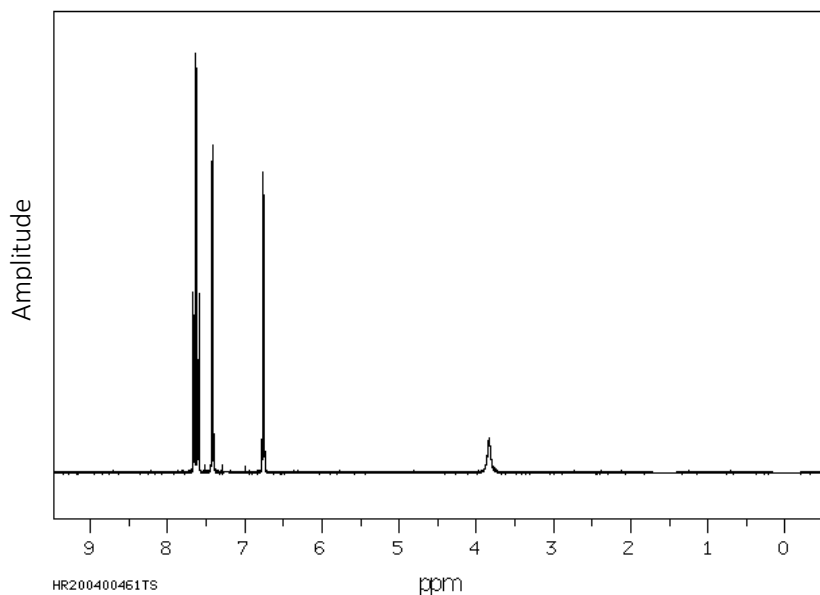
Figure 17: ¹HNMR analysis for the protonated 4-aminobiphenyl.

3.1.2 Synthesis of the partially deuterated ligand

To synthesize the ligand, deuterated 4-aminobiphenyl (BiA) was combined with protonated pyridine-2-aldehyde (PM). The reaction was conducted using the following reagents: 1.63 g of deuterated 4-aminobiphenyl (white powder), 1.46 g of pyridine-2-aldehyde (yellow liquid), and 5 drops of acetic acid (colorless liquid) in 200 mL of ethanol (colorless liquid). The reaction mixture was placed in a conical flask and connected to a reflux condenser with magnetic stirring. The temperature was set at 86°C for 2 hours, after which the reaction was allowed to cool to room temperature (RT). The solvent was then evaporated using a rotary evaporator to remove the ethanol.

Then the residue was transferred to a fume hood, where 220 mL of diethyl ether was added at 40°C, and the mixture was stirred for 1.5 hours. The flask was then placed in a freezer and left overnight to allow for crystallization. A brown-red solid product was observed, after filtration on the next day, and was air-dried for 24 hours. The final product was collected and weighed, yielding 1.14 g of material with a yellow-to-gold coloration.

The NMR spectrum was recorded using two different analyses, ^{1}HNMR in $CDCl_3$ and ^{2}HNMR (DNMR) in $CHCl_3$, to detect the signs of deuteration. The deuterated chloroform analysis revealed several key proton signals. Figure 18 shows the proton peaks. The signal at 7.26 ppm corresponds to the residual $CDCl_3$ solvent, while peaks at 7.4, 7.8, 8.7, and 8.2 ppm correspond to aromatic protons of pyridine-2-aldehyde.

The peak at 7.65 ppm represents the remaining non-deuterated proton from 4-aminobiphenyl, which corresponds to 4 protons from the biphenyl. The signals for the other 5 protons overlap with one of the signals from the pyridine ring at 7.4 ppm.

To estimate the degree of deuteration, the integration area of all peaks corresponding to aminobiphenyl was calculated to be (0.35+0.04)/9=0.043 (0.04 instead of 1.04 since the signal at 7.4 ppm also contains one proton from the pyridine ring, and 9 represents the number of protons obtainable in the non-deuterated one). Hence, the deuteration degree is 1-0.043 = 0.957 (i.e., the degree of deuteration is 95.7%).
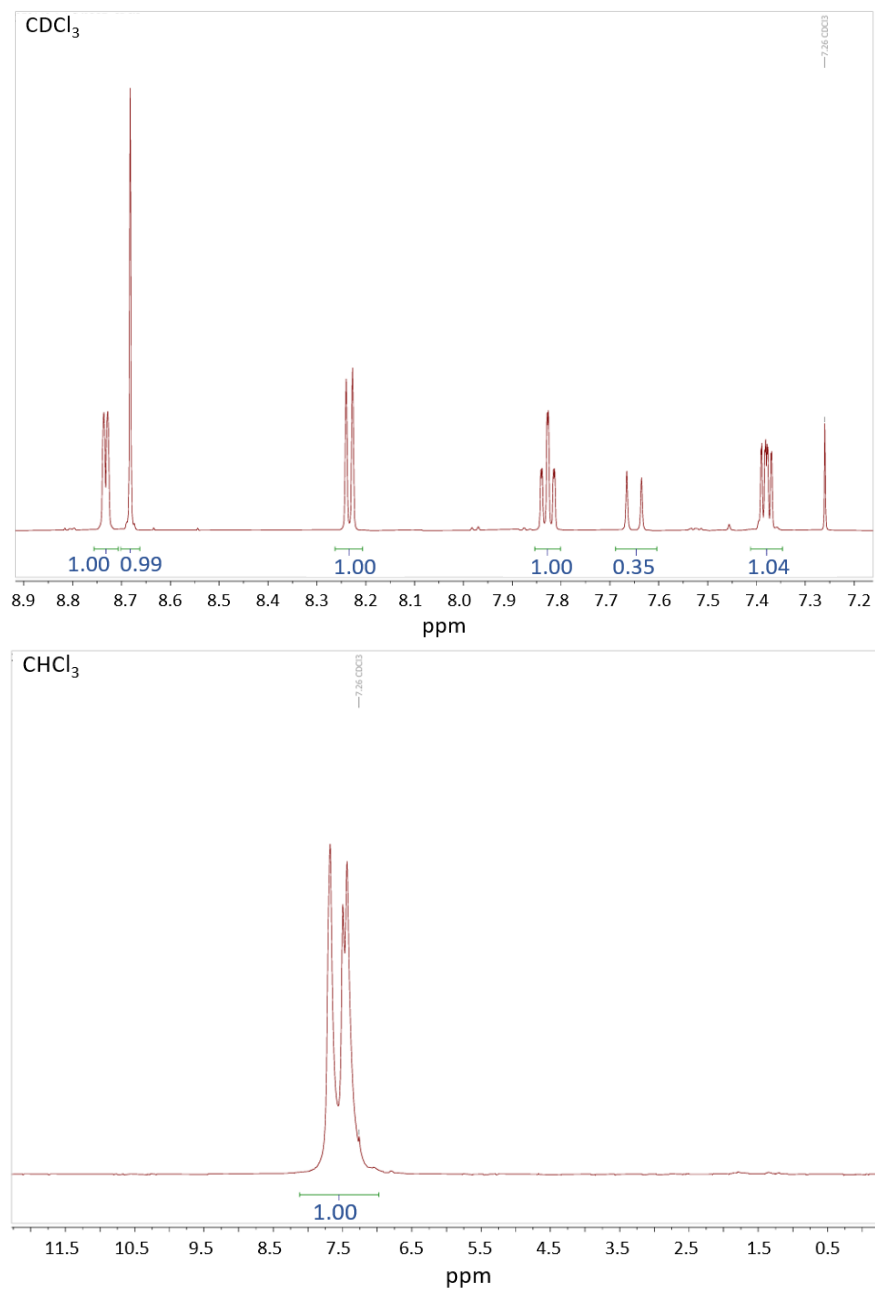
Figure 18: The NMR analysis for the partial deuterated ligand (pyridine-2-aldehyde and deuterated 4-aminobiphenyl). a) ^1H NMR in CDCl$_3$ showing several peaks for proton signals. b) ^2HNMR (NMR) in CDCl$_3$ captures the amount of deuterium incorporated in the ligand, since no proton signals appear in this spectrum, but a clear deuterium signal at 7.6 ppm is present, this indicates that the deuteration is highly efficient, which confirms that deuterium has replaced hydrogen at this position in this compound.

3.1.3   Synthesis of Partial Deuterated complex Fe(NCS)$_2$(PM-BiA)$_2$

The sample preparation of both polymorphs is prepared depending on the method mentioned there [34], for orthorhombic sample, the procedure done under usage of liquid nitrogen via schlenk line, by using (0.13867g, 4.987   mmol FeSo$_4$.7H$_2$O), potassium thiocyanate (0.10007g, 1.03 mmol KSCN) and half spatula of ascorbic acid, to prevent iron oxidation, putting them in a round-bottom storage flask with stopcock-equipped septum-inlet called number1, then adding 15 ml methanol with stirring by magnetic stir, the white product of flask 1 was filtered via a celite filter tube connected to Schlenk line, to separate the white precipitate of potassium sulfate K$_2$SO$_4$ from a colorless solution of Fe(NCS)$_2$ that needed for preparation, in another flask number with 3 connected to the schlenk line and insert in an oil bath with thermometer, a partial deuterated ligand PM-BiA was added, with (0.26653 g, 2 mmol) C$_{12}$D$_9$N-C$_6$H$_5$N, by dissolve it with 15 ml methanol, then start heating at 50 °C with stirring, after that, using the syringe to transfer the transparent solution of Fe(NCS)$_2$ drop by drop to flask 3, the color instantly will changed to dark blue by the first drop, with stirring for 2 hours, cool the mixture down to room temperature, filter it through filter paper and let it dried on air with washing the flask 3 by 5 ml of methanol and diethyl ether, the product name JQ 38 refers to orthorhombic Fe(NCS)$_2$(PM-BiA)$_2$ with partial deuterated ligand have a dark blue-black color of 0.30 g with 85% yield. This method is called slow precipitation.

The same procedure was repeated for the monoclinic one, with fast precipitation, including the stirring for one hour of flask 3 with partial deuterated ligand without heating (with no oil path), then transferring the transparent solution of Fe(NCS)$_2$ dropwise by syringe, with stirring for 1 hour, then filtering it, resulting in 0.29 grams with dark green color.

3.1.4 Deuteration of Pyridine-2-aldehyde

The main goal for deuterated pyridine-2-aldehyde is to form a fully deuterated complex. Many reactions were done to synthesize protonated pyridine-2-aldehyde from many starting materials, and if it is successful, we will apply this process to the deuterated starting material to get deuterated pyridine-2-aldehyde.

▪ The first attempt was to find a procedure for oxidizing 2-piclion to produce pyridine-2-aldehyde by the catalyst (NH$_4$)$_3$[CrMo$_6$O$_{18}$(OH)$_6$]·7H$_2$O [62]. This reaction is illustrated in Figure 19. Following the reaction, thin-layer chromatography (TLC) analysis was conducted, but no product formation was observed.
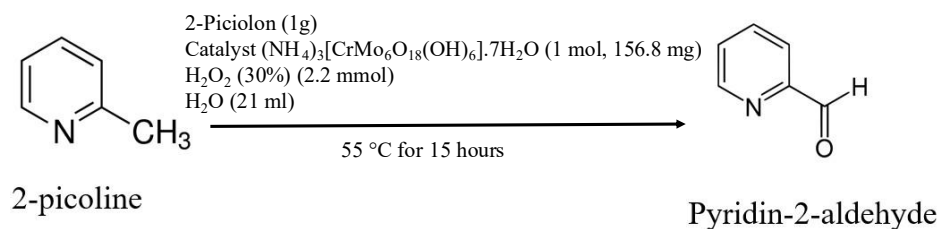
Figure 19: Synthesizing the pyridine-2-aldehyde from 2-picoline.

- The second attempt contains 3 consecutive reactions as shown in Figure 20. This attempt works well by starting with picolinic acid to synthesize the pyridine-2-aldehyde (PM), the result is confirmed by NMR analysis. We intend to repeat this reaction by using deuterated Picolinic acid to reach deuterated PM. The reactions are as follows:
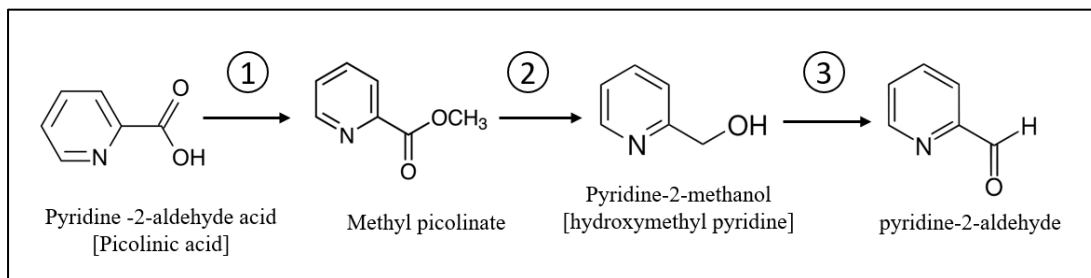
Figure 20: The consecutive reaction to obtain the protonated pyridine-2-aldehyde.

① **Synthesis of methyl picolinate from picolinic acid (pyridine carboxylic acid)**
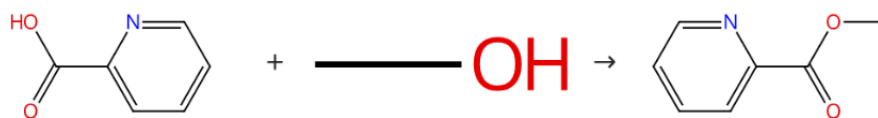
For this step [63], we start by placing 12 mmol (1.477 g) of picolinic acid (white powder) with 60 mL of methanol (colorless) in a 200 mL round-bottomed flask and add 4 mL of concentrated sulfuric acid (colorless) dropwise is added to the mixture under vigorous stirring, then allow the solution to reflux overnight and cool it to room temperature. Afterwards, the methanol from the rotary evaporator is removed to obtain the oil. Later, dissolve the oil in ethyl acetate (60 mL), then extract the mixture with saturated aqueous sodium carbonate (3x30 mL), followed by saturated sodium chloride

(1x30 mL), and dry the organic layer over anhydrous magnesium sulfate (white powder). Next, filter the organic layer before solvent removal. As a final step, dry the residue under vacuum to obtain the product, which is 1.29 grams, and the molar mass is equal to 137.736 g/mol, so the moles are equal to 9.4 mmol; hence, the yield is equal to 9.4/12 = 78%.

An NMR analysis was performed to evaluate the synthesis of methyl picolinate. The results, shown in Figure 21, indicate that peak (3) at 4 ppm corresponds to the methyl ($-OCH_3$) group in methyl picolinate. Additionally, peak (1) appears due to the aromatic protons of the pyridine ring in methyl picolinate. This means a successful synthesis of methyl picolinate. Regarding the solvent peaks, chloroform ($CDCl_3$) appears at 7.26 ppm in standard NMR spectra, which corresponds to peak (2), and peak (4) is attributed to residual methanol (CH_3OH).

Figure 21: ^1HNMR analysis for the methyl picolinate.
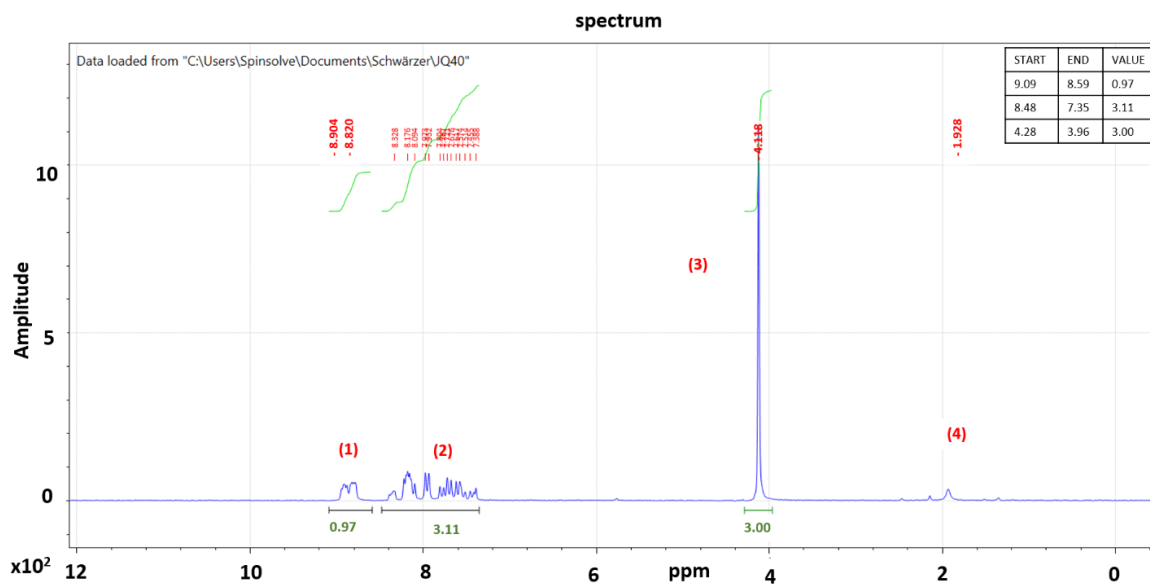
② The reduction of methyl picolinate to pyridine-2-methanol (hydroxymethyl pyridine)
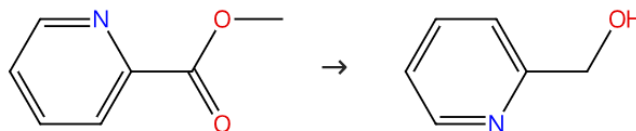
A 100 mL two-necked round-bottom flask, equipped with a magnetic stir bar and fitted with a rubber septum, equipped with the glove box, was charged with methyl picolinate (5 mmol, 0.6857 gram) (colorless), methanol (5 mL), and 5 mol % of NaOMe (0.25 mmol, 14 mg white powder) at 25 °C. Powdered NaBH$_4$ (378 mg, 10 mmol) was added in one portion to the reaction mixture with constant stirring. The progress of the reaction was followed by TLC. The mixture was stirred for 3 h at 25 °C. Then the reaction was quenched by the addition of excess methanol. After that, the resultant solution was evaporated on a rotary evaporator, and the residue was extracted with CH$_2$Cl$_2$ (5 × 10 mL). The combined extracts were dried over anhydrous sodium sulfate, and the solvent was evaporated on a rotary evaporator to obtain the crude reaction product of about 0.635 g, which is equal to 5.8 mmol of pyridine-2-methanol (colorless solution) with 70% yield [64].

The NMR pattern in Figure 22 indicates the formation of pyridin-2-methanol. Peak (1) represents the aromatic protons of the pyridine ring in pyridine-2-methanol, which are highly deshelled due to the electron-withdrawing effect of the nitrogen and hydroxyl (-OH) groups after using NaOMe. Peaks (2) and (3) correspond to other pyridine ring protons and the hydroxymethyl (-CH$_2$OH) group in pyridine-2-methanol, respectively.

The residual peaks indicate the presence of methanol from the reaction. The disappearance of the methyl ester (-OCH$_3$) peak (3.8-4 ppm) confirms the successful conversion of methyl picolinate to pyridine-2-methanol.
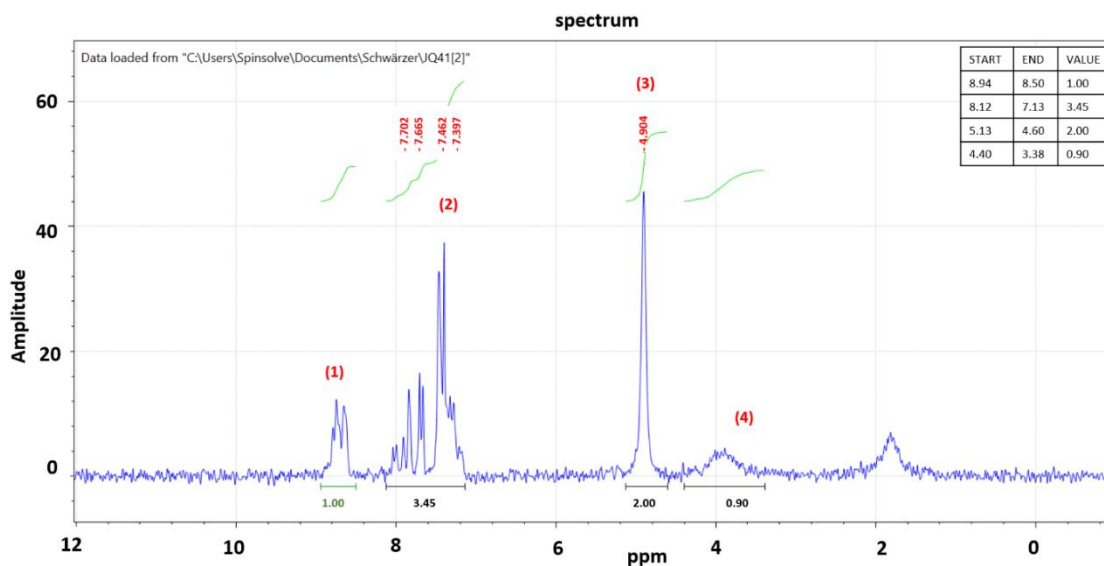
Figure 22: ^{1}HNMR analysis for the methyl picolinate.

③ **Oxidation of pyridine-2-methanol (hydroxymethyl pyridine) to pyridine-2-aldehyde**

In the glove box, the pyridine-2-methanol (0.200 g,1.8 mmol) and Dess–Martin periodinane (187 mg, 0.441 mmol, white powder) were placed in a 25 ml conical flask. Anhydrous DCM (10 mL) was added, and the mixture was stirred at room temperature for 4 hours. Three times of full peptide of Na$_2$S$_2$O$_3$(becomes colorless, tends to yellow), followed by three times of full peptide of NaHCO$_3$ (becomes a milky solution with some bubbles), were added to the solution, during stirring overnight. The organic layer was washed twice with a saturated solution of NaHCO$_3$, and the aqueous layer was

back-extracted with DCM, dried over magnesium sulfate, and filtered, then treated in vacuo to give a light-yellow liquid by 0.169 g pyridine-2-aldehyde with 1.43 mmol, with a yield of 80% [65].

An NMR analysis was performed using DMSO as a solvent, giving a clear result, as shown in Figure 23. peak (1) at 9.985 ppm is characteristic of the aldehyde proton (-CHO) in pyridine-2-aldehyde, strongly indicating the successful oxidation of pyridine-2-methanol to pyridine-2-aldehyde.

Peaks (2) and (3), observed between 8.877 and 7.736 ppm correspond to the aromatic pyridine protons. The residual peak at 2.50 ppm, labeled as peak (5), corresponds to the solvent (DMSO) used for the analysis. Additionally, the peak around 3.3 ppm, labeled as peak (4), is likely due to residual water in DMSO, which typically appears at this chemical shift due to the hygroscopic nature of DMSO.
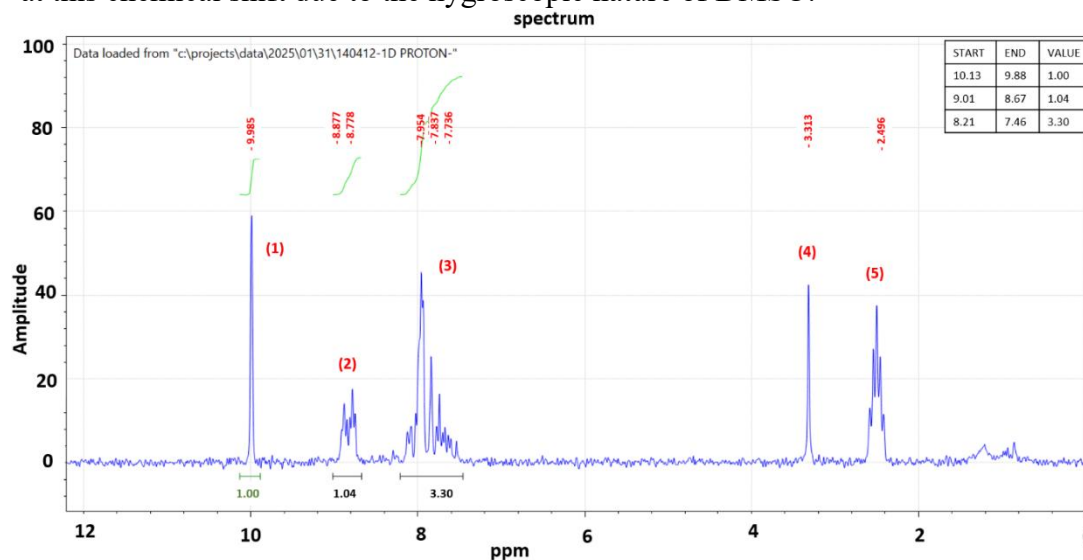
Figure 23: ¹HNMR analysis for the pyridine-2-aldehyde.

3.2 Structure proprieties of the Partial Deuterated Fe(NCS)₂(PM-BiA)₂

The primary goal of this section is to shed light on the structure properties of the partial deuterated complex and the success with which we were able to synthesize these compounds using different wavelengths, The in-house X-ray diffraction (XRD) measurements were carried out using monochromatized Cu Kα radiation ($\lambda = 1.54$Å), while synchrotron x-ray diffraction were performed with a wavelength of 0.4959 Å.

The results stipulate that the partially deuterated orthorhombic phase was successfully synthesized, with an amount of the monoclinic second phase around 26.78% (0.45). Similarly, for the partially deuterated monoclinic phase, the XRD pattern shows successful synthesis, accompanied by a 23.50% (0.55) fraction of the orthorhombic second phase as an impurity. These patterns are presented in Figure 24 for in-house measurements and Figure 25 for synchrotron measurements, at room temperature, where the impurity phases are highlighted.

Following refinement, the lattice parameter changes exhibit different behaviors depending on the crystal system. For the orthorhombic partially deuterated sample, all lattice parameters increased in both in-house and synchrotron measurements (see Tables 3 and 4). In contrast, the monoclinic sample showed minor fluctuations in the a-axis, stability in the b-axis, and a decrease in the c-axis, which corresponds to the direction of the 4-aminobiphenyl ring. This discrepancy can be attributed to differences

in density: the monoclinic phase is denser than the orthorhombic phase (ρ Ortho= 1.306 g/cm^3 (HS) and 1.3814 g/cm^3 (LS), ρ Mono= 1.3591 g/cm^3 (HS) and 1.4247 g/cm^3 (LS). The increased density in the monoclinic structure is due to tighter molecular packing. Furthermore, deuteration leads to a decrease in lattice parameters as the structure adjusts to accommodate the slightly larger deuterium atoms [66]. These findings indicate that differences in hydrogen bonding and structural packing can lead to distinct lattice parameter responses under comparable conditions.

		a (Å)		b (Å)		c (Å)		V (Å³)	
		In-house	Synch	In-house	Synch	In-house	Synch	In-house	Synch
Partial deuterated	Phase1 Ortho	12.974(4)	12.9578(8)	15.235(3)	15.1965(7)	17.698(6)	17.617(1)	3498(2)	3463.5(4)
	Phase2 Mono	17.605(4)	17.542(1)	12.623(3)	12.674(1)	17.385(3)	17.312(1)	3480(2)	3470.4(4)
Protonated	Ortho	12.949(7)		15.183(2)		17.609(5)		3339(2)	
	Mono	17.570(5)		12.602(5)		17.358(5)		3465(2)	

Table 3: Lattice parameter for the partial deuterated orthorhombic sample from in-house and synchrotron XRD measurements.

		a (Å)		b (Å)		c (Å)		V (Å³)	
		In-house	Synch	In-house	Synch	In-house	Synch	In-house	Synch
Partial deuterated	Phase1 Mono	17.600(4)	17.548(1)	12.603(3)	12.585(2)	17.333(4)	17.295(1)	3465(2)	3456.1(9)
	Phase2 Ortho	12.952(7)	12.959(2)	15.213(5)	15.191(1)	17.620(7)	17.593(2)	3480(2)	3463(1)
Protonated	Ortho	12.949(7)		15.183(2)		17.609(5)		3339(2)	
	Mono	17.570(5)		12.602(5)		17.358(5)		3465(2)	

Table 4: Lattice parameter for the partial deuterated monoclinic sample from in-house and synchrotron XRD measurements.
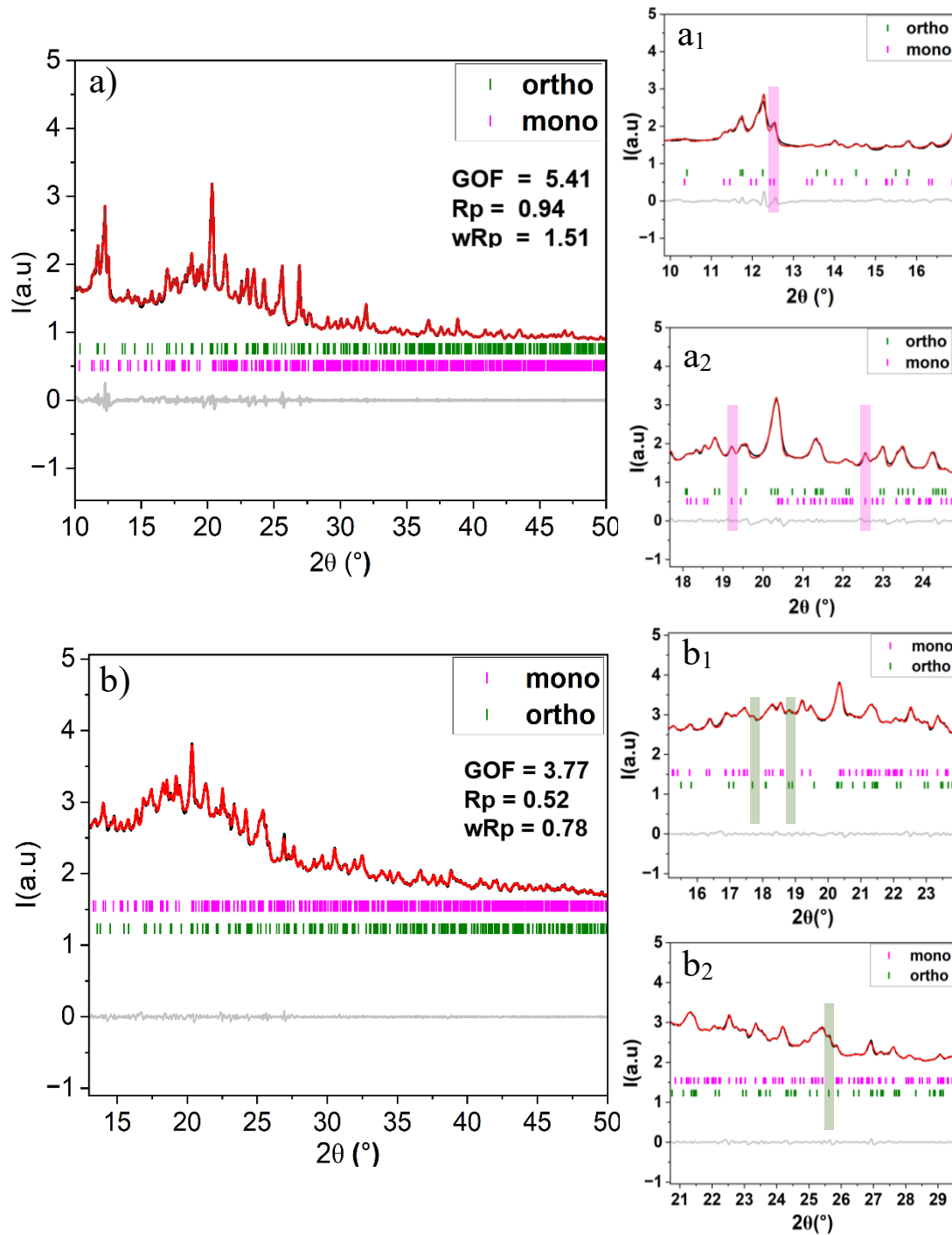
Figure 24: XRD pattern-based in-house measurements represent the impurity from the second phase for each pattern. The above is for the orthorhombic sample, which shows the impurity's peak highlighted in light pink indicated by a), a_1, and a_2, and the same situation for the monoclinic, which is highlighted in green color, marked by b), b_1, and b_2.

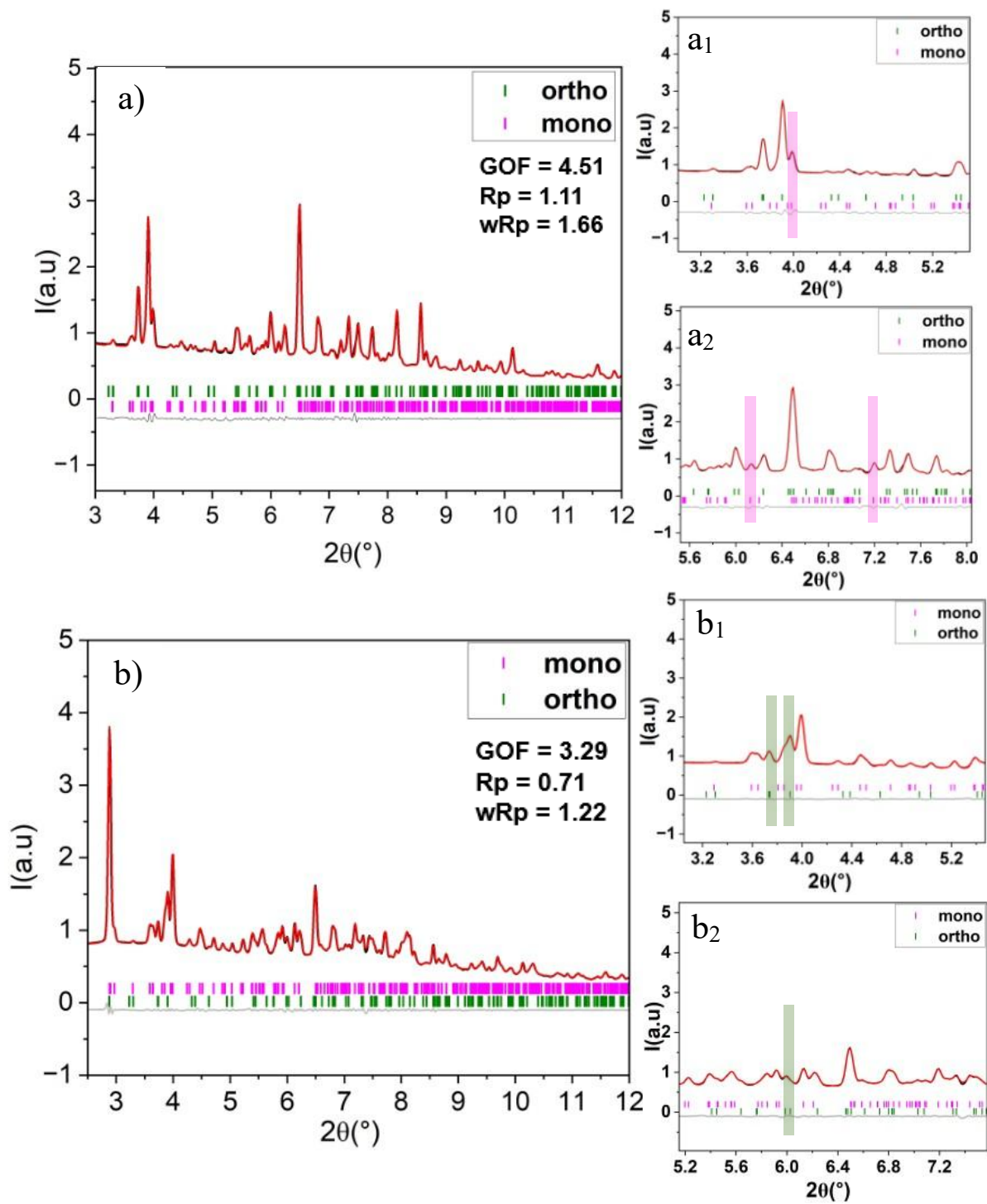*Figure 25: XRD pattern-based Synchrotron measurement that shows the 2nd phase/impurity for each sample, the above for the orthorhombic sample which shows the impurity's peak highlighted light pink, indicated by a), a_1, and a_2, and the same situation for the monoclinic, which is highlighted by green color, marked by b), b_1, and b_2.*

3.3 Deuteration Effect on the Magnetic Properties

The magnetic properties were studied by comparing with the protonated sample of both polymorphs at room temperature with 1,2,5,10, and 20 K/min scan rates as seen in Figure 26. In the orthorhombic sample, a second phase is observed, which means that the substitution of deuterium could induce a second phase, as observed in a paper published in [67]. But regarding the presence of impurities in both complexes (approximately 25%), the PD-ortho (partial deuterated orthorhombic) complex initially exhibits P-ortho-like behavior (protonated orthorhombic) during the transition, which then shifts to P-mono-like behavior (protonated monoclinic). A comparable trend is observed in the partially deuterated monoclinic (PD-mono) sample, where the transition begins with P-ortho-like features and gradually evolves into P-mono-like behavior.

For confirming the transition temperature, the HS fraction curves were listed in Figure 27 for orthorhombic and Figure 28 for monoclinic, representing the protonated and partially deuterated samples for heating and cooling modes. As observed from the magnetic behavior at a high-spin fraction (γ_{HS}) of 0.5, the transition temperature for the PD-ortho increases by 3 K compared to the P-ortho during the cooling mode. In the heating mode, the transition temperature is nearly the same, differing by only 1 K, except at a scan rate of 1 K min^{-1}. At this scan rate at $\gamma_{HS} = 0.5$, the transition shifts to monoclinic behavior, indicating that this point cannot provide reliable information about the transition temperature of PD-ortho.

In the monoclinic case, the behavior differs notably. First, all scan rates exhibit a clear spin transition characteristic of the monoclinic phase at $\gamma_{HS}= 0.5$, indicating that the $T_{\frac{1}{2}}$ of the PD-mono can be determined with confidence. Second, both heating and cooling modes reveal a reduction in the transition temperature by approximately 4 K compared to the P-mono complex. This shift in transition temperature is clearly illustrated in Figure 29 and is further supported by the data presented in Tables 5 and 6.

Several factors may account for the differences in behavior between the PD-ortho and PD-mono systems. One possible explanation is that deuteration lowers the energy barrier for the transition from the LS to the HS state, resulting in a reduced transition temperature in the monoclinic system. However, as previously demonstrated, the orthorhombic system exhibits a different response. This discrepancy may stem from changes in the reduced mass due to deuterium substitution, which in turn influences the frequencies of lattice vibrational modes, as discussed in Section 1.5.2 [68]. An alternative explanation involves the role of deuterated positions in hydrogen bonding. When deuteration occurs at sites directly participating in hydrogen bonds, the $T_{\frac{1}{2}}$ tends to increase. In contrast, when the deuterated positions are not involved in hydrogen bonding, the impact on the transition temperature is minimal [69].
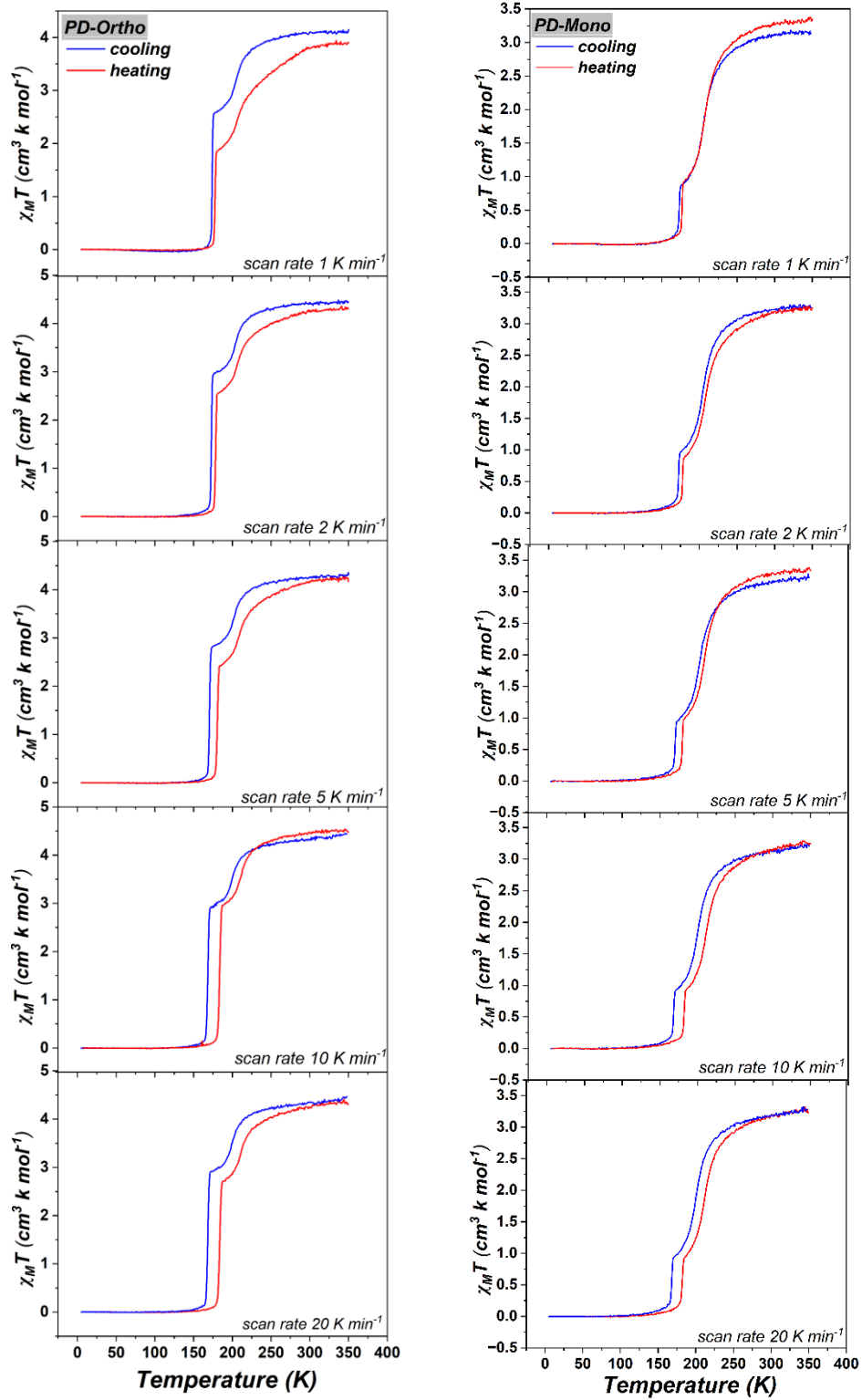
Figure 26: χm.T vs. temperature for the partial deuterated with two polymorphs: orthorhombic (left) and monoclinic (right) by five different scan rates.

—
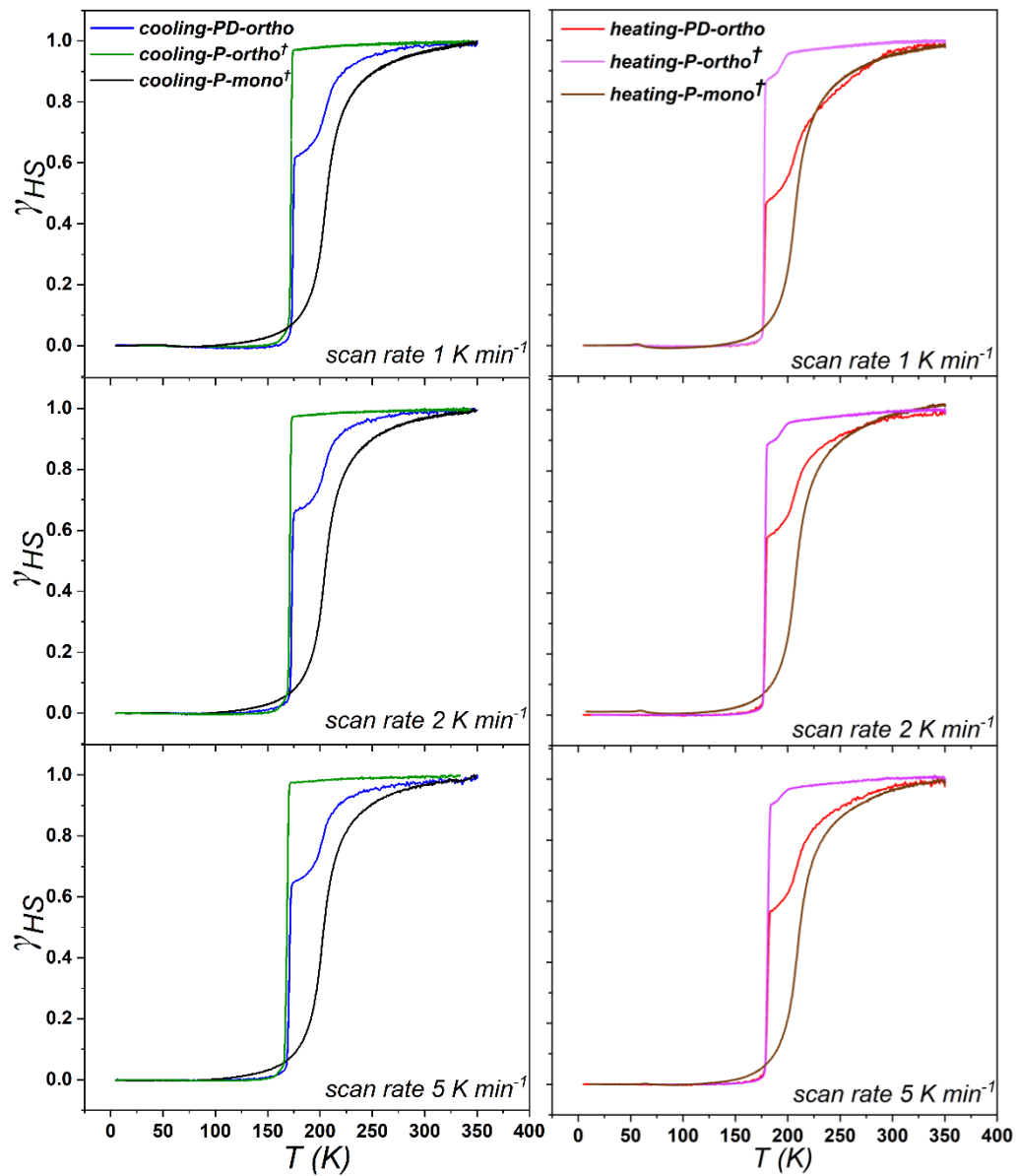
Figure 27: HS fractions for orthorhombic in both cases (PD refers to partial deuterated, P refers to protonated)
† Reference: H.Shahed et al. (2024) ref.9.
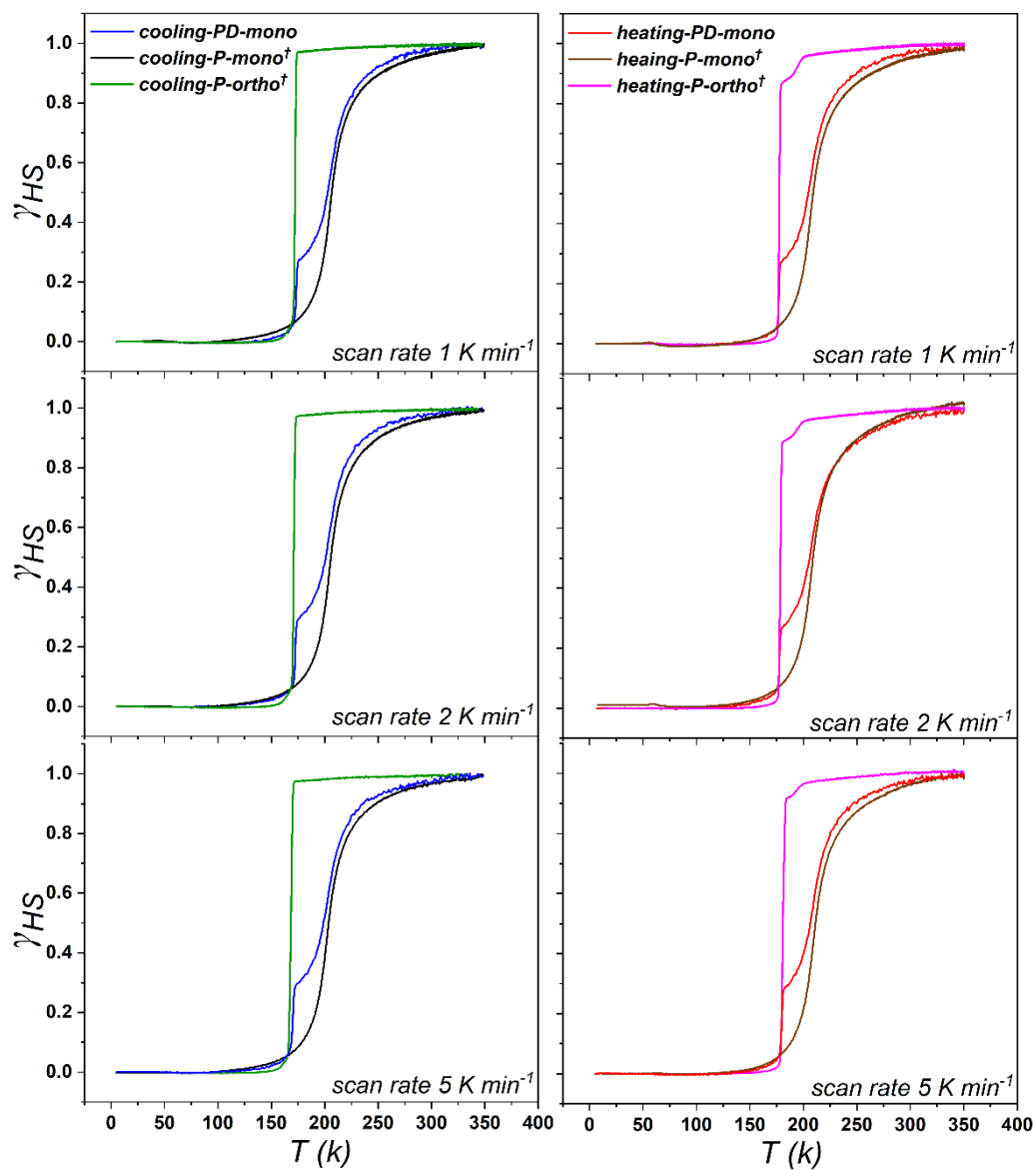
Figure 28: HS fractions for monoclinic in both cases (PD refers to partial deuterated, P refers to protonated)
† Reference: H.Shahed et al. (2024) ref.9.
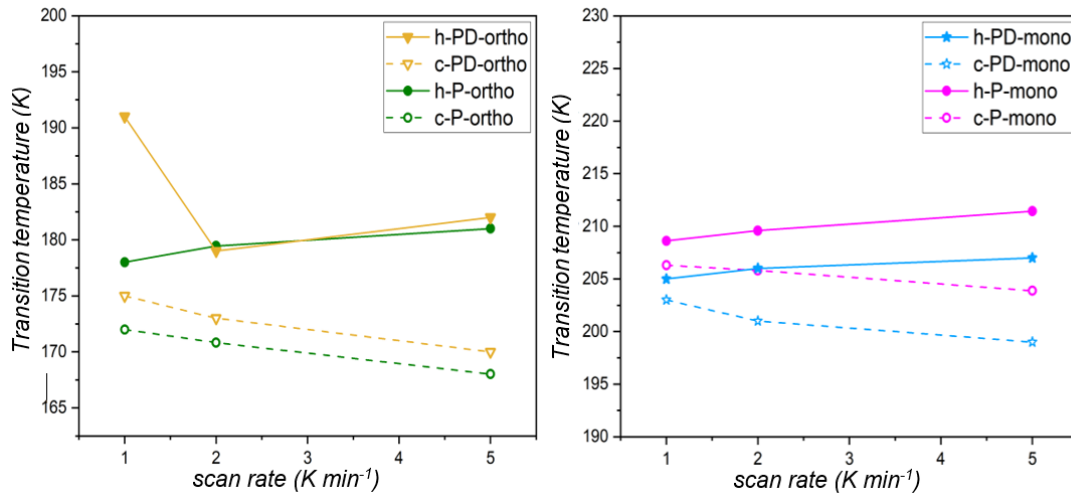
Figure 29: Scan rate vs. temperature of spin transition for both samples protonated and partial deuterated.

Scan rate (Kmin^{-1})	T$_{1/2}$ - heating P-Ortho (K)	T$_{1/2}$ - cooling P-Ortho (K)	T$_{1/2}$ - heating PD-Ortho (K)	T$_{1/2}$ - cooling PD-Ortho (K)	Hysteresis of PD-Ortho (K)
1	178	172	191	175	16
2	179	171	179	173	6
5	181	168	182	171	11

Table 5: Transition temperature values of PD-Ortho for 3 different scan rates compared to the protonated one.

Scan rate (Kmin^{-1})	T$_{1/2}$ - heating P-Mono (K)	T$_{1/2}$ - cooling P-Mono (K)	T$_{1/2}$ - heating PD-Mono (K)	T$_{1/2}$ - cooling PD-Mono (K)	Hysteresis of PD-Mono (K)
1	208	206	205	203	2
2	209	205	206	201	5
5	211	203	207	199	8

Table 6: Transition temperature values of PD-Mono for 3 different scan rates compared to the protonated one.

3.4 Deuteration Effect on the Thermodynamic Properties

The data from DSC defines each step of the transition separately, showing distinct, independent peaks without merging, besides the presence of impurities. Both complexes exhibit well-separated peaks in the plot of heat flow versus temperature. One set of peaks corresponds to monoclinic behavior, while the other corresponds to orthorhombic behavior.

The DSC measurements were performed at various scan rates (1, 2, 5, 10, and 20 K·min^{-1}). Figure 30 shows the data collected at higher scan rates for both samples, with sample masses of 7.072 mg for the orthorhombic phase and 10.758 mg for the monoclinic phase. At these higher scan rates, the two peaks are visible, particularly in the low-temperature range (step 2), which corresponds to the ortho behavior, and the high-temperature range (step 1), associated with the mono behavior; the ortho-related peaks are very sharp, indicating an abrupt transition, while the mono-related peaks are smoother, referring to a gradual transition.

At lower scan rates (1 and 2 K·min^{-1}), the orthorhombic transition peak remains visible. In contrast, the monoclinic transitions appear less distinct, manifesting as broad and smooth curves without well-defined boundaries. Minor noise-related peaks originating from the instrument are also observed, as illustrated in Figure 31.

To evaluate the enthalpy and entropy changes, measurements were conducted for both polymorphs at a scan rate of 10 K·min^{-1} and compared with those of the non-deuterated

samples, based on Equation (3.1). As previously noted, both polymorphs contain approximately 25% impurities, which influence the heat flow and, consequently, the accuracy of the thermodynamic parameters. Table 7 summarizes the enthalpy and entropy values obtained at 10 K·min⁻¹ for both deuterated and non-deuterated forms. By summing the contributions from steps 1 and 2 of the transition, the deuterated orthorhombic sample exhibited a 20–30% reduction in both enthalpy and entropy, while the monoclinic form showed a more pronounced decrease of approximately 40–50%.

$$\Delta H = \int_{T_1}^{T_2} \frac{dQ}{dT} dT = \int_{T_1}^{T_2} \frac{\frac{dQ}{dt}}{\frac{dT}{dt}} dT \tag{3.1}$$

$$= [\frac{J}{sec.g} \cdot \frac{60\,sec}{(value\ of\ the\ scan\ rate)K} \cdot g.\,K\,]$$

Figure 30: DSC curves of the orthorhombic (left) and the monoclinic (right), recorded by the high scan rate of 20, 10, and 5 Kmin⁻¹.

The reduction may be attributed to several factors. Deuterium, being twice as heavy as hydrogen, lowers vibrational frequencies and zero-point energy, thereby reducing the internal energy difference between spin states [68]. Additionally, when deuterium replaces hydrogen involved in hydrogen bonding, it weakens cooperativity during the

spin transition. Reduced cooperativity leads to smaller entropy changes due to less collective structural rearrangement [30],which may explain the greater reduction observed in the monoclinic phase compared to the orthorhombic one.

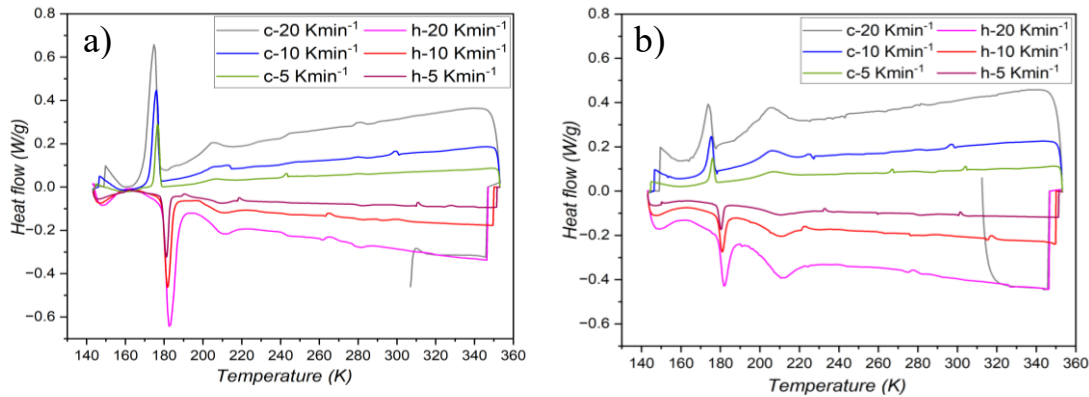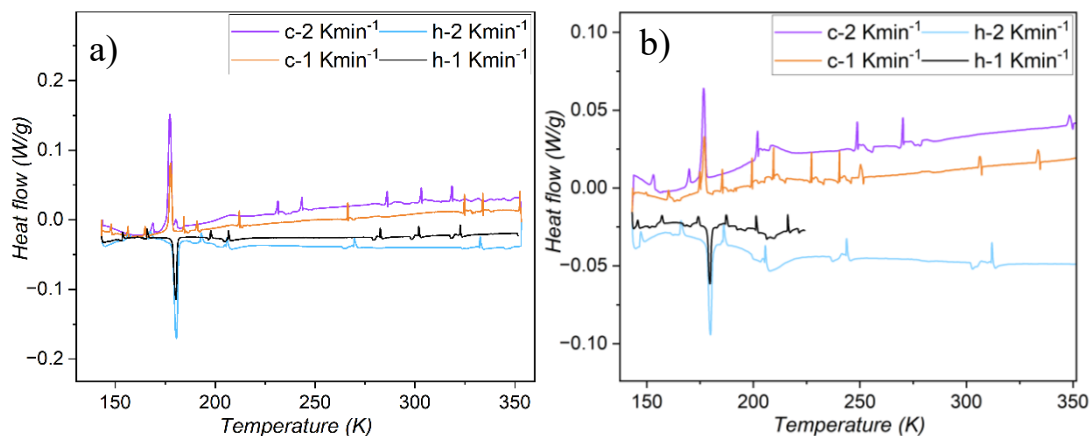*Figure 31: DSC curves of the orthorhombic (left) and the monoclinic (right), recorded by the low scan rate of 1 and 2 Kmin⁻¹.*

PD	ΔH-step1 (kJ mol^{-1}) $\uparrow$	$\downarrow$	ΔH-step2 (kJ mol^{-1}) $\uparrow$	$\downarrow$	ΔS-step1 (J mol^{-1} K^{-1}) $\uparrow$	$\downarrow$	ΔS-step2 (J mol^{-1} K^{-1}) $\uparrow$	$\downarrow$
Ortho	1.2(3)	1.4(1)	6.7(1)	7.6(2)	5.1(1)	9.3(6)	36.6(1)	40.6(1)
Mono	2.1(2)	2.0(2)	2.5(6)	2.4(4)	10.1(6)	16.7(9)	14.5(3)	22.1(2)

	ΔH-sum (kJ mol^{-1}) $\uparrow$	$\downarrow$	ΔS-sum (J mol^{-1} K^{-1}) $\uparrow$	$\downarrow$
PD-Ortho	7.9(3)	9.0(2)	42.1(1)	49.9(6)
PD-Mono	4.6(6)	4.4(4)	24.6(7)	38.8(9)
P-Ortho	10.7(3)	11.5(2)	61.3(6)	63.7(7)
P-Mono	9.7(6)	10.0(9)	47.1(3)	48.0(4)

Table 7: The values of the entropy and enthalpy for the partially deuterated sample and the protonated one. †
Reference: H.Shahed et al. (2024).

To further investigate step 2, related to the monoclinic transition, DSC measurements were performed at a fixed scan rate of 10 K·min⁻¹ while varying the final temperature from 183 K to 193K, 203K, 213K, 223K, 233K, and up to 350K. As shown in Figure 32, the orthorhombic (left) and monoclinic (right) responses indicate that the step 1 transition occurs at a consistent temperature, unaffected by changes in the maximum temperature.
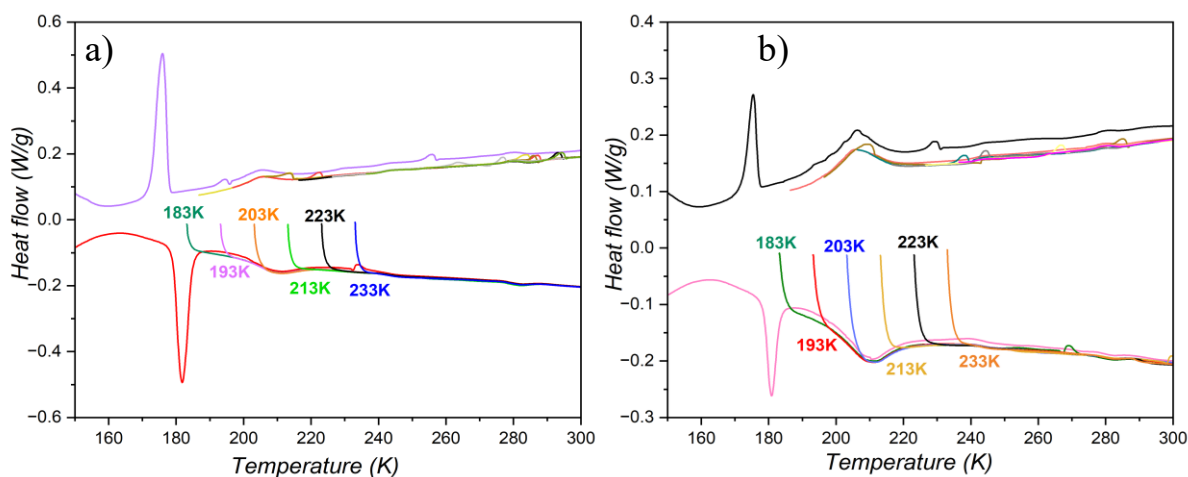

Figure 32: Different final temperatures from 183K to 350K with a fixed scan rate of 10K/min applied to capture a response that would happen at step 2. a) for orthorhombic and b) for monoclinic.

Chapter 4: Conclusion and Outlook

In this study, a partially deuterated ligand, comprising deuterated 4-aminobiphenyl and protonated pyridine-2-aldehyde, was successfully synthesized, achieving an overall deuteration level of 95.7%. The resulting $Fe(NCS)_2(PM-BiA)_2$ complex crystallized in both orthorhombic and monoclinic forms, with XRD revealing 26.78% monoclinic impurity in the orthorhombic phase and 23.50% orthorhombic impurity in the monoclinic phase. Lattice parameter analysis showed an overall expansion in the orthorhombic structure, while in the monoclinic form, the a-axis changed slightly, b remained nearly constant, and c decreased, likely due to differences in unit cell volume.

The magnetic data exhibit that the transition temperature of the partially deuterated orthorhombic phase increases by 2-3 degrees in the cooling mode and by similar values in the heating mode. In contrast, the monoclinic shows a decrease of 3-4 degrees in both modes when compared with the protonated one. This behavior may be attributed to the effect of deuteration, which lowers the energy required for the spin transition, consistent with the significant entropy reduction observed in DSC data, thereby reducing $T_{1/2}$ in the monoclinic case. In contrast, the increase in $T_{1/2}$ for the orthorhombic phase may result from changes in reduced mass affecting lattice vibrations or the involvement of deuterated sites in hydrogen bonding.

The first calorimetric measurements revealed two distinct peaks: one corresponding to the primary phase and the other to the impurity. At slower scan rates, these peaks,

particularly those associated with the monoclinic behavior, became less distinguishable compared to those observed at higher scan rates. Additionally, the total enthalpy (ΔH) of the partially deuterated orthorhombic compound was found to be 7.9 kJ mol^{-1} (heating) and 9.0 kJ mol^{-1} (cooling), while the entropy change (ΔS) was 42.1 J mol^{-1} K^{-1} (heating) and 49.9 J mol^{-1} K^{-1} (cooling). These values are approximately 30–20% lower than those of the protonated compound. As for the partially deuterated monoclinic compound, the enthalpy (ΔH) was 4.6 kJ mol^{-1} (heating) and 4.4 kJ mol^{-1} (cooling), and the entropy changes were (ΔS) 24.6 J mol^{-1} K^{-1} (heating) and 38.8 J mol^{-1} K^{-1} (cooling), showing a reduction of about 40–50% compared to the protonated counterpart. This could be attributed to the mass of deuterium, which leads to lower zero-point energy, or replacing the hydrogen position with deuterium reduces the cooperativity, which leads to a smaller entropy change.

Therefore, the transition temperature is affected by three factors:

1- The existence of the impurities, which influence all the characterization measurements and data.

2- The deuterated part of the ligand forms a partially deuterated ligand and polymorphs, which represent the primary goal of this study.

3- The scan rates used during measurements significantly influence the transition behavior, as reflected in the variation of transition temperature with different scan rates.

Based on the data and the analysis, additional investigations are required to confirm the findings. Some steps are proposed for the outlook and future work:

- Repeat the synthesis of the partially deuterated polymorphs to achieve higher purity and repeat all characterization techniques and measurements to ensure the accuracy of the result.

- Synthesize single crystals of each polymorph, further to the powder forms, to conduct the in-depth structural study. This will allow for more investigation of the bonding environments and the effects resulting from the involvement of deuterium substitution.

- Synthesize the full deuterated ligands and their corresponding polymorphs to figure out the response of the system to deuterium substitution and to isolate the isotope effect.

These steps will open avenues to a better understanding of the role of deuteration and further consistency in the interpretations presented in this thesis.

References

[1] J. L. Rodríguez-Muñoz, J. M. Belman-Flores, V. Pérez-García, A. Gallegos-Muñoz, C. Rubio-Maya, and S. Méndez-Díaz, "Energetic and Exergetic Performance Comparison of a Compression-Absorption System Working with NH_3-H_2O, NH_3-$LiNO_3$ and NH_3-NaSCN," J. Adv. Therm. Sci. Res., vol. 6, pp. 58–70.

[2] Washington, D.C.: Joseph Henry Press "A Century of Innovation: Twenty Engineering Achievements that Transformed our Lives"

[3] X. Moya, S. Kar-Narayan, and N. D. Mathur, "Caloric materials near ferroic phase transitions," Nat. Mater., vol. 13, no. 5, pp. 439–450.

[4] Seo, Jinyoung, Jason D. Braun, Vidhya M. Dev, and Jarad A. Mason. "Driving Barocaloric Effects in a Molecular Spin-Crossover Complex at Low Pressures "Journal of the American Chemical Society 144, no. 14 (2022): 6493-6503.

[5] V. Ksenofontov, A. B. Gaspar, and P. Gütlich, "Pressure Effect Studies on Spin Crossover and Valence Tautomeric Systems," in Spin Crossover in Transition Metal Compounds III, P. Gütlich and H. A. Goodwin, Eds., Berlin, Heidelberg: Springer, pp. 23–64.

[6] Miller, Reece G., Suresh Narayanaswamy, Jeffery L. Tallon, and Sally Brooker. "Spin crossover with thermal hysteresis in cobalt (II) complexes and the importance of scan rate." New Journal of Chemistry 38, no. 5 (2014): 1932-1941.

[7] A. V. Shokurov et al., "Spin Crossover in Nickel(II) Tetraphenylporphyrinate via Forced Axial Coordination at the Air/Water Interface," Molecules, vol. 26, no. 14, Art. no. 14.

[8] P. Gütlich and H. A. Goodwin, "Spin Crossover—An Overall Perspective," in Spin Crossover in Transition Metal Compounds I, P. Gütlich and H. A. Goodwin, Eds., Berlin, Heidelberg: Springer.

[9] H. Shahed et al., "Structural insight into the cooperativity of spin crossover compounds," Acta Crystallogr. Sect. B Struct. Sci. Cryst. Eng. Mater., vol. 79, no. 5, pp. 354–367.

[10] P. Gütlich, H. Köppen, and H. G. Steinhäuser, "Deuterium isotope effect on the high-spin α low-spin transition in deuterated solvates of tris(2-picolylamine) iron(II) chloride," Chem. Phys. Lett., vol. 74, no. 3, pp. 475–480.

[11] Castellanos, Maria Monica, Arnold McAuley, and Joseph E. Curtis. "Investigating Structure and Dynamics of Proteins in Amorphous Phases Using Neutron Scattering" Computational and structural biotechnology journal 15 (2017): 117-130.

[12] H. Bethe, "Termaufspaltung in Kristallen," Ann. Phys., vol. 395, no. 2, pp. 133–208.

[13] J. H. Van Vleck, "Theory of the Variations in Paramagnetic Anisotropy Among Different Salts of the Iron Group," Phys. Rev., vol. 41, no. 2, pp. 208–215.

[14] Van Vleck, J. H. "Valence Strength and the Magnetism of Complex Salts"" The Journal of Chemical Physics 3, no. 12 (1935): 807-813.

[15] C. Erkey, "Chapter 1 - Introduction to Coordination Compounds," in Supercritical Fluid Science and Technology, vol. 1, C. Erkey, Ed., in Supercritical Fluids and Organometallic Compounds, vol. 1. , Elsevier, 2011, pp. 1–10.

[16] Li, Hang, Li Wang, Youzhi Song, Yingqiang Wu, Hao Zhang, Aimin Du, and Xiangming He. "Understanding the Insight Mechanism of Chemical-Mechanical Degradation of Layered Co Free Ni-Rich Cathode Materials : a review." Small 19, no. 32 (2023): 2302208.

[17] P. Gütlich, Y. Garcia, and H. A. Goodwin, "Spin crossover phenomena in Fe(II) complexes," Chem. Soc. Rev., vol. 29, no. 6, pp. 419–427.

[18] "Lee-JD-Concise-inorganic-Chemistry_lee-5ed 2014."

[19] "Miessler and Tarr (2013), Inorganic Chemistry, 5th ed, 117-165, 475-534.

[20] L. Cambi and L. Szegö, "Über die magnetische Susceptibilität der komplexen Verbindungen," Berichte Dtsch. Chem. Ges. B Ser., vol. 64, no. 10, pp. 2591–2598, 1931

[21] W. A. Jr. Baker and H. M. Bobonich, "Magnetic Properties of Some High-Spin Complexes of Iron(II)," Inorg. Chem., vol. 3, no. 8, pp. 1184–1188.

[22] E. König and K. Madeja, "Unusual magnetic behaviour of some iron(II)–bis-(1,10-phenanthroline) complexes," Chem. Commun. Lond., no. 3, pp. 61–62.

[23] J. Linares, E. Codjovi, and Y. Garcia, "Pressure and Temperature Spin Crossover Sensors with Optical Detection," Sensors, vol. 12, no. 4, pp. 4479–4492.

[24] T. Kitazawa, "Synthesis and Applications of New Spin Crossover Compounds," Crystals, vol. 9, no. 8, Art. no. 8.

[25] O. Kahn and C. J. Martinez, "Spin-Transition Polymers: From Molecular Materials Toward Memory Devices," Science, vol. 279, no. 5347, pp. 44–48.

[26] D. Savard, C. Cook, G. D. Enright, I. Korobkov, T. J. Burchell, and M. Murugesu, "Gradual spin crossover behaviour in a linear trinuclear FeII complex," CrystEngComm, vol. 13, no. 16, pp. 5190–5197.

[27] P. Gütlich, A. B. Gaspar, and Y. Garcia, "Spin state switching in iron coordination compounds," Beilstein J. Org. Chem., vol. 9, no. 1, pp. 342–391.

[28] S. Lakhloufi, A. Kaiba, M.-H. Lemée-Cailleau, J. Létard, and P. Guionneau, "Single-crystal diffraction investigation of the transition mechanism in a gradual spin-crossover molecular material," Acta Crystallogr. A, vol. 66, pp. s253–s253.

[29] S. Yergeshbayeva, J. J. Hrudka, M. Jo, M. Gakiya-Teruya, M. W. Meisel, and M. Shatruk, "Abrupt Spin Transition in a Heteroleptic Fe(II) Complex with Pendant Naphthalene Functionality," Inorg. Chem., vol. 61, no. 29, pp. 11349–11358.

[30] P. Gütlich and H. A. Goodwin, Spin Crossover in Transition Metal Compounds II, vol. 234. in Topics in Current Chemistry, vol. 234. Berlin, Heidelberg: Springer.

[31] R. G. Miller et al., "Pressure induced separation of phase-transition-triggered-abrupt vs. gradual components of spin crossover," Dalton Trans., vol. 44, no. 48, pp. 20843–20849.

[32] J. A. Real et al., "Two-step spin crossover in the new dinuclear compound [Fe(bt)(NCS)2]2bpym, with bt = 2,2'-bi-2-thiazoline and bpym = 2,2'-bipyrimidine: experimental investigation and theoretical approach," J. Am. Chem. Soc., vol. 114, no. 12, pp. 4650–4658.

[33] H. Köppen, E. W. Müller, C. P. Köhler, H. Spiering, E. Meissner, and P. Gütlich, "Unusual spin-transition anomaly in the crossover system [Fe(2-pic)$_3$]Cl$_2$·EtOH," Chem. Phys. Lett., vol. 91, no. 5, pp. 348–352.

[34] J.-F. Létard et al., "Spin Crossover Properties of the [Fe(PM-BiA)$_2$(NCS)$_2$] Complex – Phases I and II," Monatshefte Für Chem. Chem. Mon., vol. 134, no. 2, pp. 165–182.

[35] J.-F. Létard et al., "Structural, Magnetic, and Photomagnetic Studies of a Mononuclear Iron(II) Derivative Exhibiting an Exceptionally Abrupt Spin Transition. Light-Induced Thermal Hysteresis Phenomenon," Inorg. Chem., vol. 37, no. 17, pp. 4432–4441.

[36] M. Marchivie, P. Guionneau, J.-F. Létard, and D. Chasseau, "Towards direct correlations between spin-crossover and structural features in iron(II) complexes," Acta Crystallogr. B, vol. 59, no. 4, pp. 479–486.

[37] S. Scheiner and M. Čuma, "Relative Stability of Hydrogen and Deuterium Bonds," J. Am. Chem. Soc., vol. 118, no. 6, pp. 1511–1521.

[38] X. Zhong, A. Nag, J. Zhou, K. Takada, M. Kusano, and T. Kaneko, "Pin-point Surgery of Proton-deuterium Substitution to Enhance Polybenzimidazole Thermoresistances," Chem. Lett., vol. 52, no. 10, pp. 819–822.

[39] M. M. Castellanos, A. McAuley, and J. E. Curtis, "Investigating Structure and Dynamics of Proteins in Amorphous Phases Using Neutron Scattering," Comput. Struct. Biotechnol. J., vol. 15, pp. 117–130.

[40] P. Rejnhardt, J. K. Zaręba, A. Katrusiak, and M. Daszkiewicz, "Deuteration-Enhanced Negative Thermal Expansion and Negative Area Compressibility in a Three-Dimensional Hydrogen Bonded Network," Chem. Mater., vol. 35, no. 13, pp. 5160–5167.

[41] A. Bousseksou, L. Tommasi, G. Lemercier, F. Varret, and J.-P. Tuchagues, "Deuterium isotope effect in the two-step spin-state transition of [FeII(5-NO2-sal-N(1,4,7,10))] investigated by Mössbauer spectroscopy and magnetic susceptibility," Chem. Phys. Lett., vol. 243, no. 5, pp. 493–499.

[42] B. Hutchinson, J. Takemoto, and K. Nakamoto, "Metal isotope effect on metal-ligand vibrations. II. Tris complexes of 2,2'-bipyridine and 1,10-phenanthroline," J. Am. Chem. Soc., vol. 92, no. 11, pp. 3335–3339.

[43] S. P. Vallone et al., "Giant Barocaloric Effect at the Spin Crossover Transition of a Molecular Crystal," Adv. Mater., vol. 31, no. 23.

[44] J. M. Holland, J. A. McAllister, Z. Lu, C. A. Kilner, M. Thornton-Pett, and M. A. Halcrow, "An unusual abrupt thermal spin-state transition in [FeL2][BF4]2 [L = 2,6-di(pyrazol-1-yl)pyridine]," Chem. Commun., no. 6, pp. 577–578,.

[45] R. Clausius, The Mechanical Theory of Heat: With Its Applications to the Steam-engine and to the Physical Properties of Bodies. J. Van Voorst, 1867.

[46] I. K. Howard, "H Is for Enthalpy, Thanks to Heike Kamerlingh Onnes and Alfred W. Porter," J. Chem. Educ., vol. 79, no. 6, p. 697.

[47] A. Bousseksou, G. Molnár, and G. Matouzenko, "Switching of Molecular Spin States in Inorganic Complexes by Temperature, Pressure, Magnetic Field and Light: Towards Molecular Devices," Eur. J. Inorg. Chem., vol. 2004, no. 22, pp. 4353–4369.

[48] G.Molnár, et al.,"Vibrational Spectroscopy of Cyanide-Bridged, Iron(II) Spin-Crossover Coordination Polymers: Estimation of Vibrational Contributions to the Entropy Change Associated with the Spin Transition" The Journal of Physical Chemistry B 106, no. 38 (2002): 9701-9707.

[49] M. Sorai and S. Seki, "Phonon coupled cooperative low-spin 1A1high-spin 5T2 transition in [Fe(phen)$_2$(NCS)$_2$] and [Fe(phen)$_2$(NCSe)$_2$] crystals," J. Phys. Chem. Solids, vol. 35, no. 4, pp. 555–570.

[50] A. Bousseksou et al., "Raman spectroscopy of the high- and low-spin states of the spin crossover complex Fe(phen)2(NCS)2: an initial approach to estimation of vibrational contributions to the associated entropy change," Chem. Phys. Lett., vol. 318, no. 4, pp. 409–416.

[51] M.Wasif and A.Sabieh "Studying Phase Transitions with a Strain Gage." LUMS School of Science and Engineering (2010).

[52] T. Sauer, "A Look Back at the Ehrenfest Classification. Translation and Commentary of Ehrenfest's 1933 paper introducing the notion of phase transitions of different order," Eur. Phys. J. Spec. Top., vol. 226.

[53] M. Gaeta et al., "Magnetism of materials: theory and practice in magnetic resonance imaging," Insights Imaging, vol. 12, no. 1, p. 179.

[54] R. L. Carlin and A. J. van Duyneveldt, "Paramagnetism: The Curie Law," in Magnetic Properties of Transition Metal Compounds, R. L. Carlin and A. J. van Duyneveldt, Eds., Berlin, Heidelberg: Springer, 1977, pp. 1–22.

[55] Z.-F. Guo郭, K. Pan潘, and X.-J. Wang王, "Electrochromic & magnetic properties of electrode materials for lithium ion batteries," Chin. Phys. B, vol. 25, p. 017801.

[56] .Shukla, B.Ashish, et al., "Simultaneous improvement of kinetics and thermodynamics based on SrF 2 and SrF 2@ Gr additives on hydrogen sorption in MgH 2." Materials Advances 2, no. 13 (2021): 4277-4290.

[57] Pynn, Roger. "Neutron scattering—a non-destructive microscope for seeing inside matter." Neutron applications in earth, energy and environmental sciences (2009): 15-36. [58] A. L. Bail, "Whole powder pattern decomposition methods and applications: A retrospection," Powder Diffr., vol. 20, no. 4, pp. 316–326.

[59] "Quantum Design Physical Property Measurement System (PPMS) DynaCool" Accessed: May 09, 2025. [Online]. Available: https://qdusa.com/products/dynacool.html

[60] G. A. Bain and J. F. Berry, "Diamagnetic Corrections and Pascal's Constants," J. Chem. Educ., vol. 85, no. 4, p. 532.

[61] E. Ghanbari, S. J. Picken, and J. H. van Esch, "Analysis of differential scanning calorimetry (DSC): determining the transition temperatures, and enthalpy and heat capacity changes in multicomponent systems by analytical model fitting," J. Therm. Anal. Calorim., vol. 148, no. 22, pp. 12393–12409.

[62] C. Zhao, Y. Xie, D. Shi, and H. Yu, "Selective Oxidation of Alkylarene in H2O Catalyzed by the Polyoxometalate Supported Chromium Catalyst," ChemCatChem, vol. 15, no. 11, p. e202300186.

[63] J. M. dos Santos Filho and M. V. B. de Souza Castro, "Synthesis, structural characterization, and antimicrobial activity of novel ferrocene-N-acyl hydrazones designed by means of molecular simplification strategy Celebrating the 100th anniversary of the birth of Professor Paulo Freire," J. Organomet. Chem., vol. 979, p. 122488.

[64] P. C. P. et al., "Stabilization of NaBH4 in Methanol Using a Catalytic Amount of NaOMe. Reduction of Esters and Lactones at Room Temperature without Solvent-Induced Loss of Hydride," J. Org. Chem., vol. 83, no. 3, pp. 1431–1440.

[65] S. Ulrich, E. Buhler, and J.-M. Lehn, "Reversible constitutional switching between macrocycles and polymers induced by shape change in a dynamic covalent system," New J. Chem., vol. 33, no. 2, pp. 271–292.

[66] M. Mookherjee, J. Tsuchiya, and A. Hariharan, "Crystal structure, equation of state, and elasticity of hydrous aluminosilicate phase, topaz-OH ($Al_2SiO_4(OH)_2$) at high pressures," Phys. Earth Planet. Inter., vol. 251, pp. 24–35.

[67] A. Rotaru et al., "Hydrostatic pressure investigation of the spin crossover compound $[Fe(PM-BiA)_{(2)}(NCS)_{(2)}]$ polymorph I using reflectance detection," J. Appl. Phys., vol. 106, p. 053515.

[68] P. Gütlich, H. Köppen, and H. G. Steinhäuser, "Deuterium isotope effect on the high-spin α low-spin transition in deuterated solvates of tris(2-picolylamine) iron(II) chloride," Chem. Phys. Lett., vol. 74, no. 3, pp. 475–480.

[69] P. Gütlich and A. Hauser, "Thermal and light-induced spin crossover in iron(II) complexes," Coord. Chem. Rev., vol. 97, pp. 1–22.

Appendix A: Supplementary Comments on Magnetic Behavior

- Further analysis from magnetization data: the hysteresis between the heating and cooling modes of the transition temperature increases with faster scan rates, as shown in Figure 35. For PD-ortho, where the most left-shifted transitions appear at 20 K·min⁻¹ and 10 K·min⁻¹ in the cooling mode (colored yellow and blue) and at the far right in the heating mode (colored blue and red), as evidenced in Figure 33 and Figure 34 for the PD-mono complex
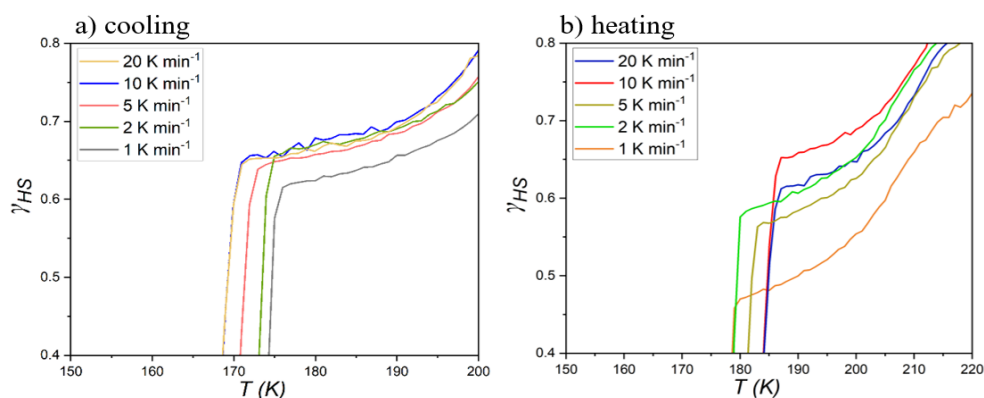

Figure 33: Transition temperature region of orthorhombic for both modes with five scan rates: 1, 2, 5, 10, and 20 Kmin⁻¹.

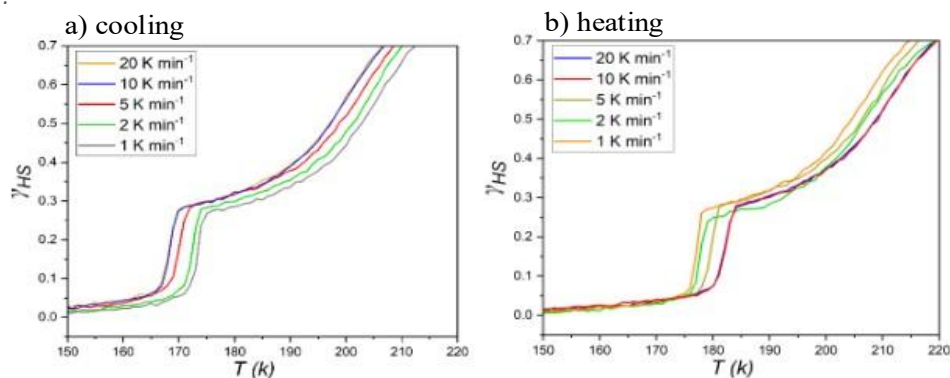*Figure 34: Transition temperature region of monoclinic for both modes with five scan rates: 1, 2, 5, 10, and 20 Kmin⁻¹.*
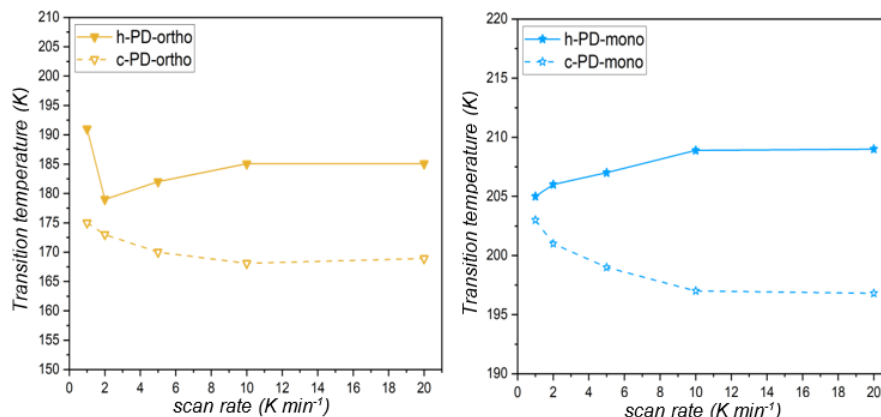
Figure 35: Scan rate vs. transition temperature for both polymorphs with five scan rates: 1, 2, 5, 10, and 20 Kmin^{-1}.

- The spin transition behavior for the partially deuterated complex vs. applying a hydrostatic pressure: Figures 36 and 37 show the transition behavior from magnetization data compared with an experiment including applying a hydrostatic pressure over a protonated sample from this paper [67]. Hydrostatic pressure compresses the molecular lattice, shortens metal–ligand bond distances, and increases orbital overlap. This enhances the ligand field splitting energy, making the HS state less favorable and stabilizing the LS state, thereby shifting the transition temperature to higher values, as more thermal energy is needed to overcome the increased energy gap. In contrast, deuteration introduces a "negative pressure" effect by increasing the mass and occupying interatomic voids. This lowers the energy required for the LS → HS transition and, together with reduced entropy change, shifts T½ to lower temperatures.
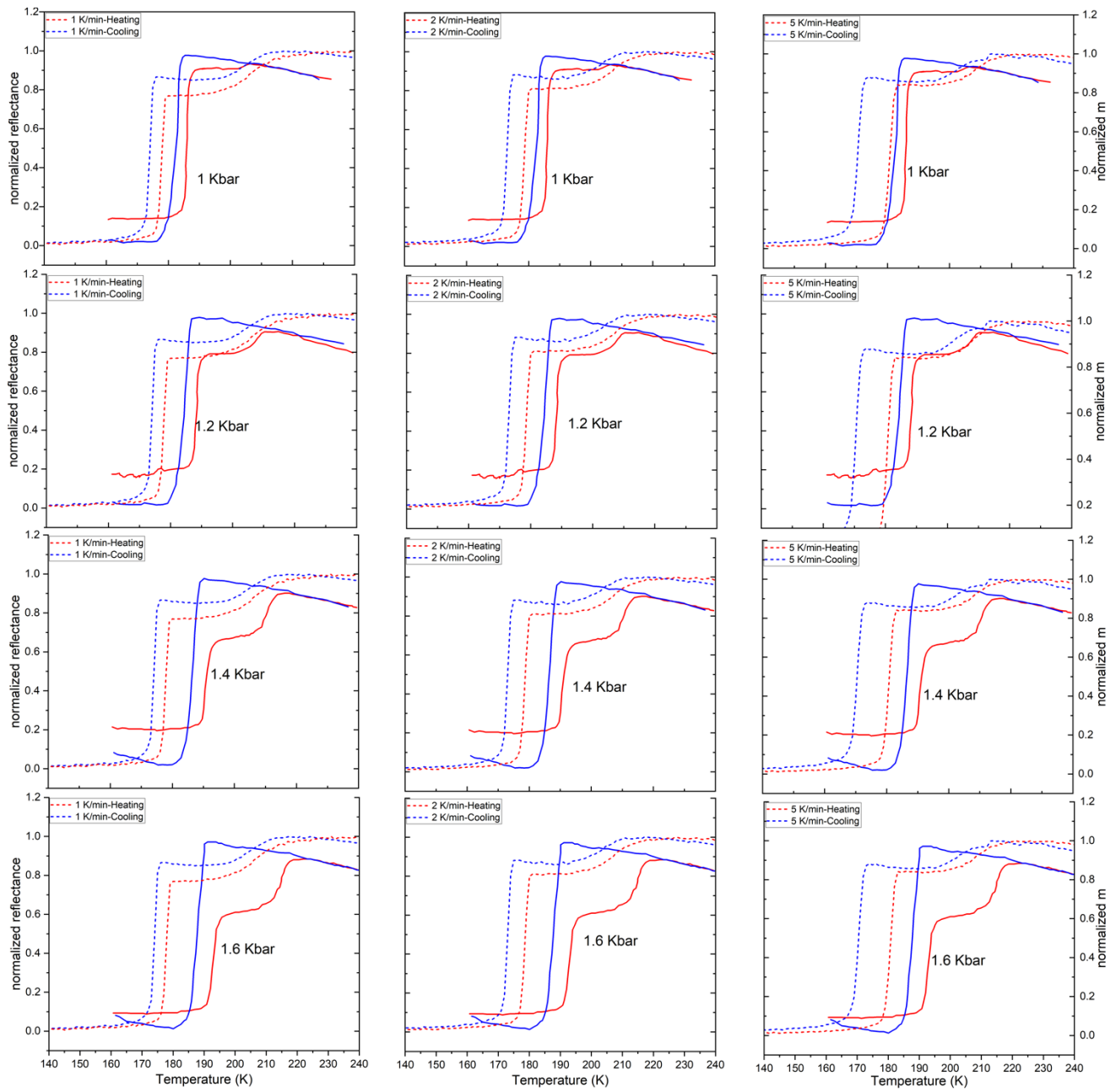
Figure 36: Comparing spin transition behavior for the partially deuterated orthorhombic (dashed line) with different scan rates vs. applying a hydrostatic pressure between 1 and 1.6 Kbar over the protonated orthorhombic one (solid line).
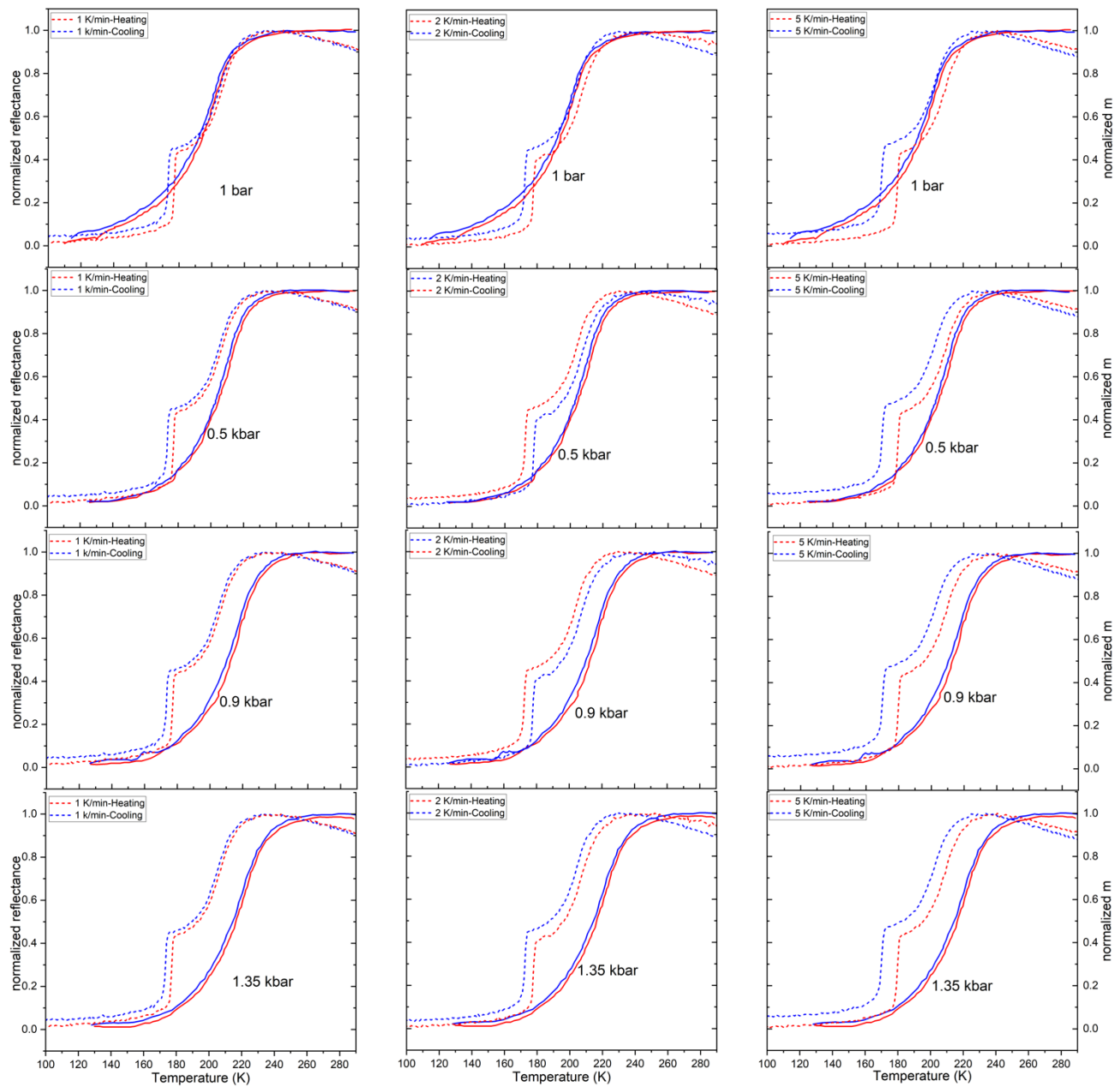
Figure 37: Comparing spin transition behavior for the partially deuterated monoclinic (dashed line) with different scan rates vs. applying a hydrostatic pressure between 1 bar and 1.35 Kbar over the protonated monoclinic one (solid line).

Appendix B: Supplementary Comments on Transition Temperature

- Comparison between the PPMS and DSC: the transition temperature cannot be extracted for the entire complex from DSC because of presenting the data is presented separately for each component. In contrast, the PPMS data reflects a bulk property, capturing the response from all atoms collectively. This is why it shows a mixed transition behavior, combining both ortho and mono transitions. In this case, the transition temperatures corresponding to each peak can be extracted from each step as observed in Figure 38 and compared with the DSC data. Figure 39 corresponds to the first step at high temperatures, where the transition temperatures do not exhibit a significant or consistent trend. On the other hand, the second step at low temperature shows a consistent increase in the transition temperature based on the PPMS data, which primarily depends on the purity of the observed peak.
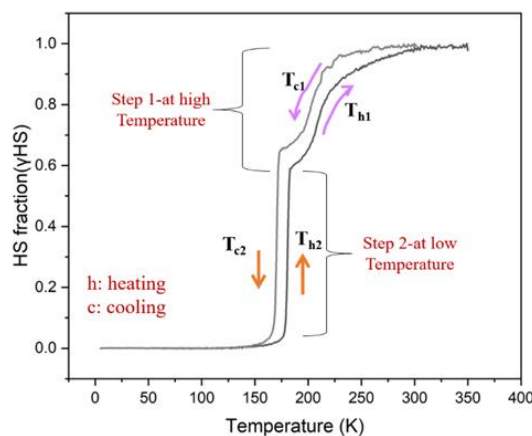
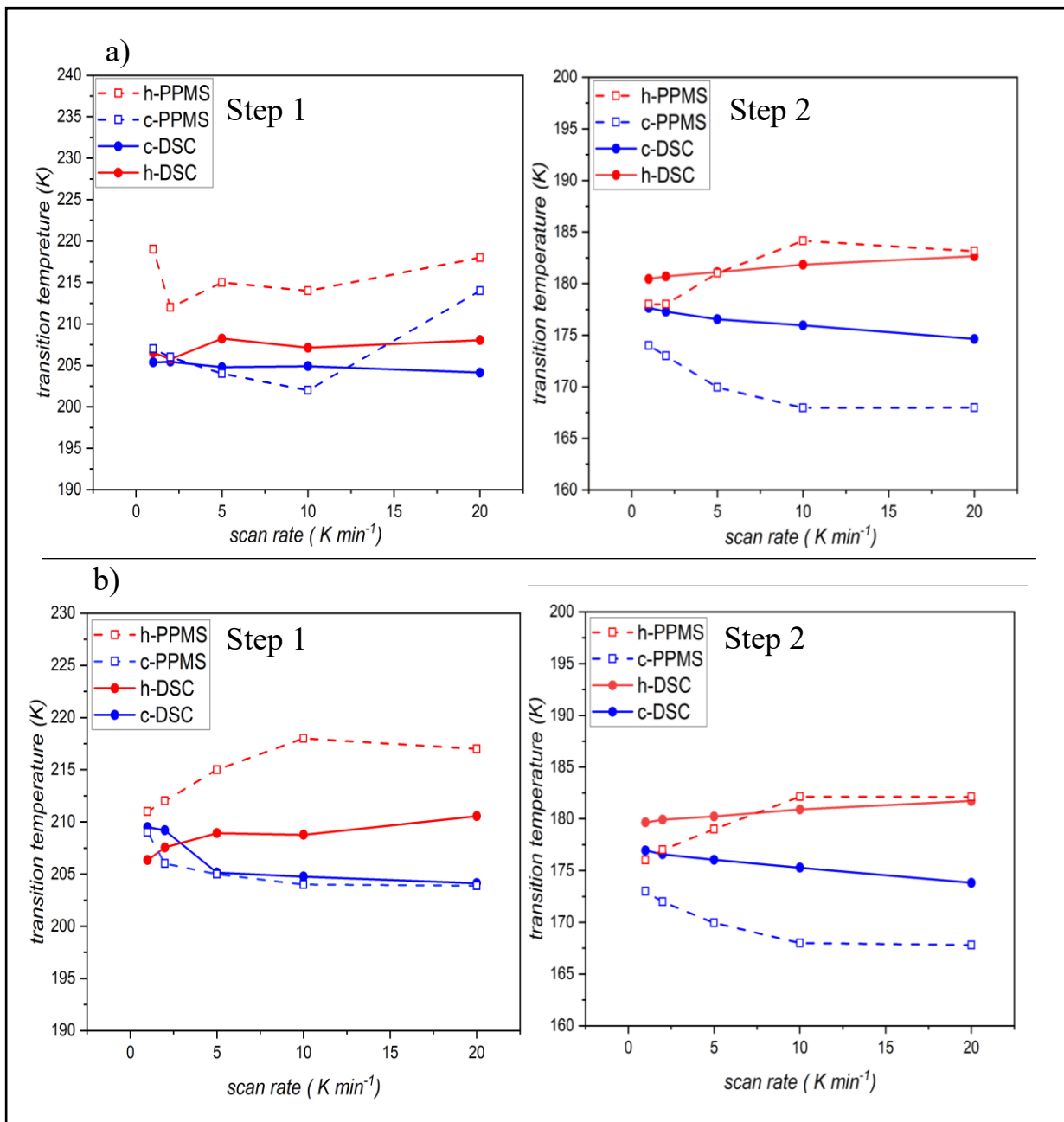*Figure 38: Representation of the 2-step transition.*

Figure 39: The transition temperature vs. scan rate for each step separately was compared between the PPMS and the DSC data; the upper figure refers to PD-orthorhombic (a), and the lower one refer to PD-monoclinic (b).